Annual Review of Marine Science

Mixing Efficiency in the Ocean

M.C. Gregg,[1] E.A. D'Asaro,[1] J.J. Riley,[2] and E. Kunze[3]

[1]Applied Physics Laboratory and School of Oceanography, University of Washington, Seattle, Washington 98105, USA; email: mgregg@uw.edu, dasaro@apl.washington.edu

[2]Department of Mechanical Engineering, University of Washington, Seattle, Washington 98195, USA; email: rileyj@u.washington.edu

[3]Northwest Research Associates, Redmond, Washington 98052, USA; email: kunze@nwra.com

Annu. Rev. Mar. Sci. 2018. 10:9.1–9.31

The *Annual Review of Marine Science* is online at marine.annualreviews.org

https://doi.org/10.1146/annurev-marine-121916-063643

Keywords

mixing efficiency, mixing coefficient, diapycnal diffusivity, differential diffusion, stratified turbulence, Kelvin-Helmholtz instability

Abstract

Mixing efficiency is the ratio of the net change in potential energy to the energy expended in producing the mixing. Parameterizations of efficiency and of related mixing coefficients are needed to estimate diapycnal diffusivity from measurements of the turbulent dissipation rate. Comparing diffusivities from microstructure profiling with those inferred from the thickening rate of four simultaneous tracer releases has verified, within observational accuracy, 0.2 as the mixing coefficient over a 30-fold range of diapycnal diffusivities. Although some mixing coefficients can be estimated from pycnocline measurements, at present mixing efficiency must be obtained from channel flows, laboratory experiments, and numerical simulations. Reviewing the different approaches demonstrates that estimates and parameterizations for mixing efficiency and coefficients are not converging beyond the at-sea comparisons with tracer releases, leading to recommendations for a community approach to address this important issue.

1. INTRODUCTION

J_b: $-\frac{g}{\rho}\overline{\rho' w'}$, where $g = 9.81$ m s^{-2} and ρ is the density

N: $\sqrt{-\frac{g}{\rho}\frac{\partial \rho}{\partial z}}$

χ_T: $2\kappa_T \overline{(\nabla \Theta')^2}$, where κ_T is the molecular thermal diffusivity and Θ is Conservative Temperature

χ_S: $2\kappa_S \overline{(\nabla S_A')^2}$, where κ_S is the molecular salt diffusivity and S_A is Absolute Salinity

ϵ: $2\nu s_{ij} s_{ji}$, where ν is the kinematic viscosity and $s_{ij} = \frac{1}{2}\left(\frac{\partial u_i}{\partial x_j} + \frac{\partial u_j}{\partial x_i}\right)$

Contrasts in velocity, temperature, and salinity imposed by air-sea interactions are ultimately dissipated throughout the ocean's interior by centimeter-scale gradients, often termed microstructure, produced by a cascade of turbulent energy from larger scales. The accompanying turbulent fluxes are parameterized in ocean models by diascalar diffusivities, e.g., diapycnal diffusivity, K_ρ, perpendicular to isopycnals; diathermal diffusivity, K_T, perpendicular to isotherms; and diahaline diffusivity, K_S, perpendicular to isohalines. The fluxes are products of the diffusivity and the corresponding mean gradient; e.g., the diapycnal buoyancy flux is represented as $J_b = -K_\rho N^2$, where N^2 is the stratification expressed as the square of the buoyancy frequency, N. Examining ocean general circulation models (OGCMs), Jayne (2009, p. 1757) stated that "parameterized vertical [diapycnal] mixing . . . is of utmost importance if OGCMs are to correctly model the ocean's circulation." In addition, mixing in the upper ocean affects horizontal circulation, meridional overturning, and poleward heat transport much more than does abyssal mixing.

The observational challenge is to estimate K_ρ, K_T, and K_S from what can be measured. Two methods are widely used to interpret microstructure observations. The first, based on scalar gradient variance, has been widely applied to temperature, estimating K_T from measurements of χ_T, the rate at which molecular heat diffusion smooths thermal gradients, scaled with the mean temperature gradient. The corresponding method for K_S has proven technologically difficult owing to the difficulty in measuring the much smaller gradients contributing to χ_S.

The second microstructure method is based on the shear variance, ϵ, the rate at which molecular viscosity smooths velocity gradients. Both methods assume, usually implicitly, that the data used to estimate diffusivities are averages during relatively steady large-scale forcing of many mixing events sampled at varying intensities and ages.

Because most mixing is produced by breaking internal waves at rates proportional to internal wave intensity, global patterns of ϵ can be estimated from internal wave characteristics over vertical scales of tens to hundreds of meters, bypassing most details of mixing events and turbulence (McComas & Müller 1981, Henyey et al. 1986, Gregg 1989, Polzin et al. 1995, Whalen et al. 2015, Kunze 2017). However, obtaining K_ρ from ϵ depends on the efficiency of the mixing, a concept that is simple in theory but difficult to apply in practice.

Estimating mixing efficiency is limited by what can be measured at sea and in laboratories and by idealizations invoked in formulating numerical simulations. This has led to the multitude of efficiency definitions discussed in the next section. Our goals are to (*a*) explain the basis for microstructure-based flux estimates and the range of turbulent conditions over which they have been verified, (*b*) point out limitations with current procedures that may be responsible for some of the scatter in estimates and lead to even larger errors in parts of the ocean, (*c*) summarize relevant laboratory and numerical results, and (*d*) recommend steps toward a unified understanding of ocean, laboratory, and numerical approaches.

2. CONCEPTS AND DEFINITIONS

The basic definition

$$\text{Mixing efficiency} \equiv \frac{\text{Change in background potential energy due to mixing}}{\text{Energy expended}} \qquad 1.$$

can be estimated from rates of change, from fluxes, and from net changes. Given perfect measurements and extensive sampling, all three should yield the same numbers. Measurements, however, are not ideal. Nor do all working definitions include all relevant parameters. Consequently,

Table 1 Definitions of efficiency, $\mathcal{E}$; coefficients, γ; and flux ratios, R, used in this review

Symbol	Expression[a]	Description
$\mathcal{E}_\mathrm{i}$	$\frac{\mathrm{d}GPE_\mathrm{r}/\mathrm{d}t-\phi_\mathrm{i}}{\mathrm{d}GPE_\mathrm{r}/\mathrm{d}t-\phi_\mathrm{i}+\epsilon}$	Instantaneous turbulent mixing efficiency
$\mathcal{E}_\mathrm{c}$	$\frac{\int(\mathrm{d}GPE_\mathrm{r}/\mathrm{d}t-\phi_\mathrm{i})\,\mathrm{d}t}{\int(\mathrm{d}GPE_\mathrm{r}/\mathrm{d}t-\phi_\mathrm{i}+\epsilon)\,\mathrm{d}t}$	Cumulative turbulent mixing efficiency
$\mathcal{E}_\mathrm{pe1}$	$\frac{\mathrm{d}GPE_\mathrm{r}/\mathrm{d}t}{\epsilon_\mathrm{turbulent}-\epsilon_\mathrm{viscous}}$	
$\mathcal{E}_\mathrm{pe2}$	$\frac{\mathrm{d}GPE_\mathrm{r}/\mathrm{d}t}{\epsilon_\mathrm{turbulent}}$	
$\mathcal{E}_\mathrm{iw}$	$\frac{\int_{t_0}^{t}(\mathrm{d}GPE_\mathrm{r}/\mathrm{d}t-\phi_\mathrm{i})\,\mathrm{d}t}{\lvert\Delta E_\mathrm{wave}\rvert_{t_0}^{t}}$	
$\mathcal{E}_{\mathrm{pe},\epsilon}$	$\frac{\gamma_{\mathrm{pe},\epsilon}}{1+\gamma_{\mathrm{pe},\epsilon}}$	
$\mathcal{E}_\mathrm{pe,nl}$	$\frac{\mathrm{d}GPE_\mathrm{r}/\mathrm{d}t\lvert_\mathrm{turbulent}}{Dape}$	Instantaneous nonlinear mixing efficiency
R_f	$\frac{-(g/\rho)\overline{w'\rho'}}{\overline{u'w'}(\partial\overline{u}/\partial z)}=\frac{J_b}{\overline{u'w'}(\partial\overline{u}/\partial z)}$	Flux Richardson number
γ_{R_f}	$\frac{R_\mathrm{f}}{1-R_\mathrm{f}}$	Mixing coefficient to obtain K_ρ from ϵ, N^2
$\gamma_{\chi\epsilon}$	$\frac{K_\rho N^2}{\epsilon}=\frac{\chi_T N^2}{2\epsilon(\partial\overline{\Theta}/\partial z)^2}$	Mixing coefficient for K_ρ if $K_T=K_\rho$
$\gamma_{\mathrm{pe},\epsilon}$	$\frac{\mathrm{d}GPE_\mathrm{r}-\phi_\mathrm{i}}{\epsilon}$	
$\hat{R}_\mathrm{f}$	$\frac{J_b}{J_b+\epsilon}$	Equilibrium approximation to R_f
R_flux	$\frac{\alpha\overline{w'\Theta'}}{\beta\overline{w'S'_\mathrm{A}}}$	Ratio of heat and salt density fluxes
$R_\mathrm{flux}^\mathrm{sf}$	$\frac{K_T^\mathrm{sf}}{K_\rho^\mathrm{sf}}=\left(\frac{R_\mathrm{flux}^\mathrm{sf}}{1-R_\mathrm{flux}^\mathrm{sf}}\right)\left(\frac{R_\rho-1}{R_\rho}\right)$	Ratio of heat and salt diffusivities for salt fingering

[a]ϕ_i is the potential energy flux produced by laminar diffusion on gradients sharpened by instabilities, e.g., on braids between Kelvin-Helmholtz billows.

Table 1 uses subscripts to distinguish between efficiencies, $\mathcal{E}$, and related coefficients, γ, needed to scale particular parameters.

2.1. Mixing Efficiency in a Linear Boussinesq Fluid

Seawater is often assumed to be a linear Boussinesq fluid with density variations affecting only buoyancy, e.g., as $\rho=\alpha(\Theta-\Theta_0)$. Potential energy then has two components: available (*APE*), which is convertible into kinetic energy, and background or gravitational (GPE_r), which is not convertible. Computed from density sorted in three dimensions to increase monotonically, GPE_r is changed only by molecular diffusion, making $\mathrm{d}GPE_\mathrm{r}/\mathrm{d}t$ the most fundamental measure of mixing rates. Integrating the Cox number over the full three-dimensional monotonic field yields $\mathrm{d}GPE_\mathrm{r}/\mathrm{d}t$ (Winters & D'Asaro 1996), but this cannot be replicated exactly with the limited data available from observations.

Using direct numerical simulations of Kelvin-Helmholtz (KH) instabilities on an interface between homogeneous layers, Peltier & Caulfield (2003) included only turbulent mixing, subtracting enhanced molecular diffusion, ϕ_i, from $\mathcal{E}_\mathrm{i}$ and $\mathcal{E}_\mathrm{c}$. For application to the pycnocline, ϕ_i should be included and bounding layers should be weakly stratified, as they usually are in the pycnocline

α: $-\frac{1}{\rho}\frac{\partial\rho}{\partial\Theta}$

(Desaubies & Gregg 1981, Pinkel & Anderson 1992), to allow propagation of internal wave energy from instabilities.

R_f: $\frac{J_b}{\overline{u'w'}(\partial\overline{u}/\partial z)}$

To estimate efficiency in a tank mixed by an oscillating paddle and lacking measurements of production, McEwan (1983a) defined $\mathcal{E}_{pe1}$ by replacing production with ϵ. Smyth et al. (2001) adapted this to $\mathcal{E}_{pe2}$ by subtracting ϕ_i and ignoring viscous dissipation. A more general approach for mixing produced by internal waves used $\mathcal{E}_{iw}$ with $|\Delta E_{wave}|$, the magnitude of energy lost by the wave field (Bouruet-Aubertot et al. 2001).

2.2. Mixing Efficiency in a Non-Boussinesq Fluid

Extending linear Boussinesq analysis to compressible fluids, Tailleux (2009a) included internal energy from expansion and contraction accompanying pressure changes and nonlinear equations of state. Neglecting laminar mixing and assuming thermal stratification,

$$\left.\frac{dGPE_r}{dt}\right|_{mixing} \approx \left.\frac{dGPE_r}{dt}\right|_{turbulent} = -\int \kappa\rho c_p \nabla T \cdot \nabla\left(\frac{\alpha_r p_r}{\rho_r c_{p,r}}\right) dV \quad (W), \qquad 2.$$

where $c_{p,r}$ is the specific heat of the reference profile. The rate of increase in GPE_r depends on the vertical gradient of the fraction of the heat received during isobaric processes that can be converted into work but not into internal energy, $\Pi(z) \equiv \alpha p/\rho c_p = p\Gamma_{adiabatic}/T$. For comparison, the dissipation rate of available potential energy is

$$Dape = -\int \frac{T - T_r}{T} \nabla \cdot (\kappa\rho c_p \nabla T)\, dV \quad (W). \qquad 3.$$

Although $dGPE_r/dt$ and $Dape$ have similar forms, Tailleux (2009a) argued that they are separate processes related by mutual dependence on molecular diffusion. For linear Boussinesq processes, this reduces to $Dape = dGPE_r/dt|_{turbulent}$, as found by Winters et al. (1995).

Because $Dape$ is largely independent of $\Pi(z)$, nonlinear potential energy variations greatly change $\mathcal{E}_{pe,nl}$ throughout the ocean. Using synthetic profiles, Tailleux (2009b) found the Boussinesq approximation to be accurate, i.e., $\mathcal{E}_{pe,nl} \approx 1$, for warm surface water, but $\mathcal{E}_{pe,nl} < 1$ as salinity and temperature decrease and pressure increases. (Including only part of expended energy, $\mathcal{E}_{pe,nl}$ has a maximum value of 1.) For example, $\mathcal{E}_{pe,nl}$ drops to 0.10 for $S_A = 30$ and $T = 1.2°C$ at the surface, and some ratios are strongly negative: $\mathcal{E}_{pe,nl} = -47.5$ for $T = 2.2°C$, $S_A = 35$, and $p = 20$ MPa ($\approx$ 2,000 m), the greatest pressure evaluated. Negative $\mathcal{E}_{pe,nl}$ indicates that mixing decreases GPE_r, the opposite of what is often assumed. Most of the variability comes from the dependence of $dGPE_r/dt|_{turbulent}$ on $\Pi(z)$. Tailleux's results imply a very different relationship between ϵ and mixing in significant parts of the ocean than is usually assumed, findings that call for further investigation.

2.3. The Flux Richardson Number, R_f

As a ratio of averages of two sets of partially correlated variables, R_f is difficult to measure, owing to large fluctuations of both numerator, $\overline{u'w'}$, and denominator, $\overline{\rho'w'}$, relative to their means. One approach uses submarines and towed bodies; another uses sensors on frames fixed to tanks, ice floes, and channels. Even so, compromises are needed, e.g., using moorings, a bottom-mounted acoustic Doppler current profiler, and transects along a tidal river. Holleman et al. (2016) had to calculate the flux Richardson number as $\hat{R}_f$, which estimates energy expended as $J_b + \epsilon$ in lieu of the total Reynolds stress production used for R_f (**Table 1**). In steady-state divergenceless flow, $\hat{R}_f$ should equal R_f, but that has not been demonstrated.

Table 2 Ratio of $\gamma^d_{\chi\epsilon}$ to $\gamma_{\chi\epsilon}$ (K_ρ to K_T) during weak mixing with $d < 1$ ($K_S < K_T$) in Pacific and Atlantic pycnoclines

	R_ρ	$\gamma^d_{\chi\epsilon}/\gamma_{\chi\epsilon}$	
		$d = 0$	$d = 0.5$
North Pacific	3.82	1.35	1.18
South Pacific	2.56	1.64	1.32
North Atlantic	1.95	2.05	1.53
South Atlantic	1.89	2.12	1.56

R_ρ values are from Schmitt (1981).

2.4. Mixing Coefficients

Although rarely measured, R_f is often termed the mixing efficiency, as distinguished from the ratio $\gamma_{R_f} \equiv R_f/(1 - R_f)$, which we refer to as a mixing coefficient (Section 3.2). Lacking γ_{R_f} but having simultaneous ϵ and χ_T measurements, Oakey (1982) assumed $K_T = K_\rho$ to obtain an alternate mixing coefficient, $\gamma_{\chi\epsilon}$, by equating Equations 9 and 11 (see below). St. Laurent & Schmitt (1999) related the two with

$$\gamma_{\chi\epsilon} = \left(\frac{R_{\text{flux}}}{R_{\text{flux}} - 1}\right)\left(\frac{R_\rho - 1}{R_\rho}\right)\gamma_{R_f}, \qquad 4.$$

where R_{flux} is the ratio of thermal and haline buoyancy fluxes (**Table 1**) and R_ρ is the density ratio. When $K_T = K_\rho$ the flux ratio equals the density ratio, $R_{\text{flux}} = R_\rho$, and $\gamma_{\chi\epsilon} = \gamma_{R_f}$.

To examine Oakey's assumption, linearized forms for the buoyancy flux and stratification can be expressed as

$$J_b \equiv -\frac{g}{\rho}\overline{w'\rho'} = -\frac{g}{\rho}\left(-\rho\alpha\,\overline{w'T'} + \rho\beta\,\overline{w'S'}\right) = -g\alpha\frac{\partial T}{\partial z}\left(K_T - \frac{K_S}{R_\rho}\right) \quad (\text{W kg}^{-1}), \qquad 5.$$

$$N^2 \equiv -\frac{g}{\rho}\frac{\partial \rho}{\partial z} = -\frac{g}{\rho}\left(-\rho\alpha\frac{\partial T}{\partial z} + \rho\beta\frac{\partial S}{\partial z}\right) = g\alpha\frac{\partial T}{\partial z}\left(\frac{R_\rho - 1}{R_\rho}\right) \quad (\text{s}^{-2}). \qquad 6.$$

To allow for weak turbulence, the ratio of haline to thermal diffusivity is given as $d \equiv K_S/K_T$. Using Equations 5 and 6 to obtain $\gamma^d_{\chi\epsilon}$ from $J_b = -\gamma^d_{\chi\epsilon}\epsilon/N^2$ then yields the ratio of the mixing coefficients for weak and strong turbulence as

$$\frac{\gamma^d_{\chi\epsilon}}{\gamma_{\chi\epsilon}} = \left(\frac{R_\rho - d}{R_\rho - 1}\right) = \frac{K_\rho}{K_T}. \qquad 7.$$

When $d = 1$, turbulence is strong, with $K_S = K_T = K_\rho$ and $\gamma^d_{\chi\epsilon} = \gamma_{\chi\epsilon}$, as expressed by Oakey. When $d < 1$, turbulence is weak, with $K_S < K_T$ and $\gamma^d_{\chi\epsilon} > \gamma_{\chi\epsilon}$; i.e., the conventional $\gamma_{\chi\epsilon}$ underestimates the ratio of K_ρ to K_T by an amount that increases as R_ρ decreases (**Table 2**). Consequently, R_ρ is an important parameter for mixing efficiency.

γ_{R_f}: $\frac{R_f}{1-R_f}$

R_ρ: $\frac{\alpha\partial\overline{\Theta}/\partial z}{\beta\partial\overline{S_A}/\partial z}$, where $\beta = \frac{1}{\rho}\frac{\partial\rho}{\partial S_A}$

Re_b: $\frac{\epsilon}{\nu N^2}$

2.5. Differential Diffusion

Mixing with $d = K_S/K_T < 1$ is known as differential diffusion. Gargett (2003) reviewed the initial studies, which began with Turner (1968) reporting faster mixing of heat compared with salt in a tank stirred with an oscillating grid. As discussed in Section 8.5, laboratory experiments

and numerical models have demonstrated $K_T \neq K_S$ where Re_b, the buoyancy Reynolds number, is less than 100, a situation found in large parts of the pycnocline. Consequently, $\gamma_{\chi\epsilon}$, based on assuming $K_T = K_S$, cannot be accurate in those places.

w': vertical velocity fluctuation

C: $\frac{K_T}{\kappa_T}$

Re: $\frac{u'l}{\nu}$

2.6. Double Diffusion

Where background shear is negligible and salinity and temperature increase upward, the ratio of haline and density diffusivities becomes the salt-fingering flux ratio, $R_{\text{flux}}^{\text{sf}}$ (Hamilton et al. 1989). Where fingering or the alternate regime of double diffusion exist (Section 6.2.2), $\gamma_{\chi\epsilon}$ is not appropriate because it lowers potential energy by releasing an unstable component of the stratification.

3. DIAPYCNAL DIFFUSIVITY FROM MICROSTRUCTURE AND TRACERS

Observationally based estimates of diascalar mixing are based on inferring diffusivities from microstructure observations assuming that rates of turbulent production balance rates of viscous and diffusive dissipation. Confidence in the technique is based on four comparisons with thickening rates of artificial tracers.

3.1. Estimating K_T Using the Osborn & Cox (1972) Method

Osborn & Cox (1972) assumed that, on average, temperature variance production balances temperature variance dissipation:

$$-\overline{w'\Theta'}\frac{\partial\overline{\Theta}}{\partial z} = \chi_T \quad (\mathrm{K^2\ s^{-1}}). \qquad 8.$$

Representing the diathermal flux with an eddy coefficient leads to

$$K_T \equiv -\frac{\overline{w'\Theta'}}{(\partial\overline{\Theta}/\partial z)} = \frac{\chi_T}{2(\partial\overline{\Theta}/\partial z)^2} = \kappa_T \frac{\overline{(\nabla\Theta')^2}}{(\partial\overline{\Theta}/\partial z)^2} \quad (\mathrm{m^2\ s^{-1}}). \qquad 9.$$

Uncertainties include the following:

1. The degree of isotropy. The one gradient component that is measured is multiplied by 3, assuming isotropy over the scales contributing to χ_T. Direct numerical simulation of this assumption reveals serious errors for Cox numbers, C, less than 10, which would be found where Reynolds numbers, Re, are low.
2. Spatial resolution of the gradients. Nearly all χ_T estimates involve some degree of correction for probe attenuation. Although attenuation differs among individual probes, corrections are usually based on nominal dynamic responses.
3. Differences in algorithms. Some χ_T estimates are obtained by integrating spectra after correction for probe response. Other estimates are derived by fitting universal spectra to the corrected spectra, but two theoretical forms have been used (Batchelor 1959, Kraichnan 1968), with different values for the empirical scaling constant, q.
4. Lateral convergence of Θ'^2 in the presence of strong lateral gradients and horizontal diffusivity (Gregg 1975, Alford et al. 2005, Ferrari & Polzin 2005).
5. Estimation of $\partial\overline{\Theta}/\partial z$. The difficulty of estimating the gradient against which overturns operate is complicated by the stratification varying irregularly in the vertical (Smyth et al. 2001) and in time with internal wave strain.

3.2. Estimating K_ρ Using the Osborn (1980) Method

Similarly to Osborn & Cox (1972), Osborn (1980) assumed a steady balance between production of turbulent kinetic energy, *TKE*; dissipation; and work against buoyancy:

$$\overline{u'w'}\frac{\partial \overline{u}}{\partial z} = J_b - \epsilon \quad (\mathrm{W\,kg^{-1}}). \qquad 10.$$

u': horizontal velocity fluctuation

A measure of mixing efficiency that is negative in stratified turbulence, the buoyancy flux, J_b, is the small difference between upward and downward fluxes resulting from molecular diffusion along the way as water parcels rise and fall. Lacking measurements of $\overline{u'w'}$, Osborn invoked the flux Richardson number, R_f, to write the *TKE* equation as $J_b(1 - R_f) = -\epsilon R_f$, yielding

$$K_\rho \equiv -\frac{J_b}{N^2} = \frac{R_f}{1 - R_f}\frac{\epsilon}{N^2} \quad (\mathrm{m^2\,s^{-1}}). \qquad 11.$$

Closely related to efficiency but not numerically the same, we denote $R_f/(1 - R_f)$ as a mixing coefficient, γ_{R_f}. Citing $R_f \approx 0.15$ from Ellison (1957), Osborn (1980) treated $\gamma_{R_f} \approx 0.2$ as an upper bound. Subsequent usage has often omitted the less-than symbol, treating efficiency as constant throughout the ocean, although it was generally understood that it may vary.

Uncertainties include the following:

1. The degree of isotropy. Direct numerical simulation of a KH instability shows errors up to a factor of 10 in ϵ estimated from only one shear component when $Re_b \lesssim 100$ (Smyth & Moum 2000), and isotropy errors are negligible (Gargett et al. 1984).
2. Platform vibration and plankton impacts. Most observations are made with airfoils (Osborn 1974), which are sensitive to vibrations and plankton hits.
3. Spatial resolution. Airfoils resolve shear in typical regions of the pycnocline but are often too large to resolve shear variance where turbulence is intense, requiring extrapolation of observed spectra using universal forms.
4. Estimation of N^2. Estimating $\overline{N^2(z)}$ in overturns is difficult and further complicated by salinity spiking resulting from mismatches in dynamic probe responses.
5. Estimation of the mixing coefficient γ_{R_f}, which is a major focus of this review.

3.3. Testing K_ρ and K_T Against Tracers

The North Atlantic Tracer Release Experiment (NATRE) found K_ρ and K_T within a factor of two of the rates at which thin tracer streaks thickened (**Table 3**). Similar results were obtained from the three other microstructure/tracer comparisons, with K_ρ varying by a factor of 33, from 5×10^{-5} m^2 s^{-1} at abyssal depths in the Brazil Basin to $0.15–0.18 \times 10^{-5}$ in the seasonal thermocline over the New England continental shelf. In all cases, K_ρ from microstructure was estimated using $\gamma_{R_f} = 0.2$, providing the primary justification for using this value. The reasons for this agreement, however, are not fully understood, nor are circumstances when it may fail.

4. SCALING MIXING WITH DIMENSIONLESS VARIABLES

In the absence of standard parameters for stratified turbulence, Mater & Venayagamoorthy (2014) used *TKE* and ϵ for the turbulence, N, and shear, S, for the environment, and κ_T and ν for the molecular properties, to which κ_S should be added. For seven variables and two fundamental units, length and time, the Buckingham π theorem yields $7 - 2 = 5$ dimensionless parameters. Consequently, mixing efficiency should be assumed to depend on multiple dimensionless parameters. In addition to the Prandtl, *Pr*; Schmidt, *Sc*; and Reynolds, *Re*, numbers, dimensionless

Table 3 Diapycnal diffusivities from thickening rates of injected tracers and microstructure

Location	Depth (m)	K_{tracer} ($\times 10^5$ m^2 s^{-1})	K_{micro} ($\times 10^5$ m^2 s^{-1})	Reference
Northeast Atlantic	300	1.1	1.1 ± 0.2[a]	Ledwell et al. 1998
Brazil Basin	4,000	5	5	Ledwell et al. 2000
Northwest Atlantic shelf	12–18	0.18 ± 0.05[b]	0.15 ± 0.05	Ledwell et al. 2004
Circumpolar Current[c]	1,500	1.3 ± 0.02	0.75 ± 0.07	Ledwell et al. 2011

The tracer was SF_6 except on the shelf, where dye was used.
[a]Sherman & Davis (1995), Toole et al. (1994).
[b]Oakey & Greenan (2004).
[c]West of Drake Passage.

choices include the buoyancy Reynolds number, Re_b; the gradient Richardson number, Ri_g; and the Froude number, Fr.

Re_b is often a surrogate for Re because ϵ is widely measured but not u'. Standard assumptions for stratified turbulence, also known as Taylor scaling, that $\epsilon \sim u'^3/l$ and $u' \sim Nl$ result in $Re_b \sim Re$ and the Ozmidov length, l_O, being the outer scale of the turbulence. The only direct comparison we are aware of shows that Re_b is highly correlated with Re but has a steeper slope and significant scatter (**Figure 1*a***); subsets of the data follow similar slopes, $Re_b \propto Re^{1.1}$, but with significant offsets. The dissipation rates follow Taylor scaling but with a significant proportionality factor, $\epsilon \approx 4u'^3/l$ (Peters et al. 1995). Consequently, the scaling assumptions are justified, but there is no rationale for using Re_b and Re interchangeably.

Noting that the length scale is assumed to be the vertical scale of the turbulence, i.e., $l = l_v$, and assuming that $S \sim u'/l_v$, Fr is sometimes used interchangeably with the inverse square root of Ri_g. Also assuming $u' \sim Nl_v$ leads to $Fr_v = u'/Nl_v \sim 1$ and $Ri_g \sim 1$ (Lilly 1983, Billant & Chomaz 2001). The assumption is reasonable for the initial stages of shear instabilities, but as the turbulence evolves, the mean shear, influenced by the large-scale background, may not change in the same way. Observations of vertical Froude numbers in **Figure 1*b*** show them clustering around 1, but with significant scatter, a further reason for not interchanging Fr and $Ri_g^{-1/2}$.

5. PYCNOCLINE STRUCTURE AND MIXING

Before efficiencies from laboratory and numerical studies can be applied to ocean observations, idealizations made in these studies must be compared with conditions in the ocean.

S: $\frac{\partial u}{\partial z}$
κ_S: molecular salt diffusivity
Pr: $\frac{\nu}{\kappa_T}$
Sc: $\frac{\kappa_S}{\nu}$
Ri_g: $\frac{N^2}{S^2}$
Fr: $\frac{u'}{Nl}$
l_O: $\left(\frac{\epsilon}{N^3}\right)^{1/2}$

5.1. Fine-Scale Stratification

The typical pycnocline is "irregularly steppy," precluding objective identification of high-gradient sheets separating homogeneous layers (Desaubies & Gregg 1981). Rather, when internal waves are at the Garrett and Munk background level and $\Delta z > 2$ m, distributions of $\Delta\Theta/\Delta z$ are consistent with formation by transient internal wave strain, as are Ri_g statistics (Desaubies & Smith 1982). Some large gradients slope across density surfaces, indicating high-frequency internal waves following inclined trajectories (Lazier 1973, Alford & Pinkel 2000). As Δz decreases below 2 m, temperature gradients become coherent, evidence that the internal wave field decays at smaller scales.

In contrast to transient pycnocline stratification and shear, most laboratory and numerical studies assume sheet-and-layer structures (Woods & Wiley 1972). Based on observations of dyed high gradients in a shallow pycnocline (Woods 1968), the model posits a pycnocline of thin, high-gradient, horizontal sheets separated by much thicker homogeneous layers. Occasional KH

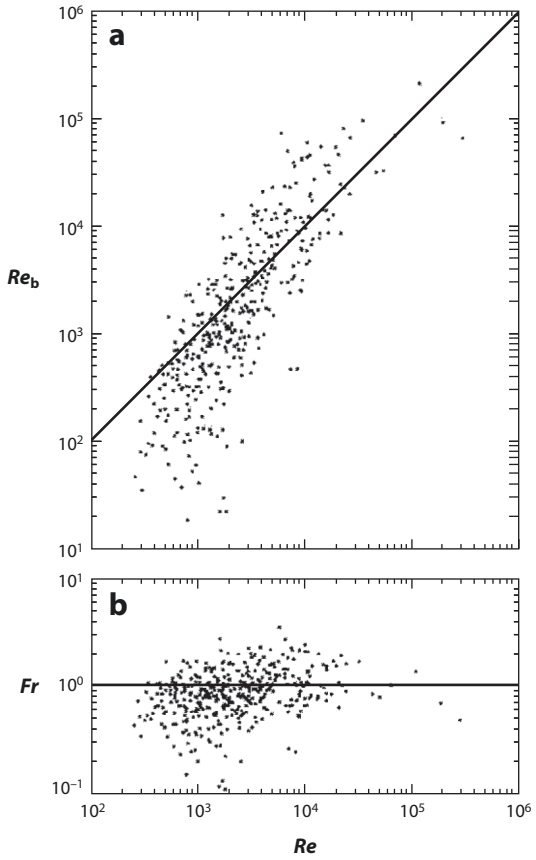

Figure 1

(*a*) Buoyancy Reynolds number, Re_b, and (*b*) vertical Froude number, Fr, versus Reynolds number, Re, in the upper 350 m on the equator at 140°W. Reynolds and Froude numbers are based on u' measured every 0.1 m in the vertical with the Multi-Scale Profiler. Re_b is highly correlated with Re, but the correlation is not 1:1 over the full range. Adapted from Peters et al. (1995).

instabilities homogenize sheets with parts of their bounding layers to produce new interfaces offset from the originals. Although this model captures aspects of pycnocline mixing, the pycnocline is far from having distinct sheets and layers. It also remains to be demonstrated whether KH is the dominant mode of mixing and whether model efficiencies replicate those driven by the most energetic internal waves. Determining the dominant mechanisms producing mixing is an essential step on the path toward parameterizing mixing efficiency.

5.2. Mixing Intensity

In background internal waves, 20–30% of the total dissipation comes from only a few percent of measurements having $Re_b \geq 200$ (Gregg & Sanford 1988), a range that is isotropic at dissipation scales (Gargett et al. 1984). Roughly half of ϵ comes from 10–20% of the data with intermediate intensity, $16 \lesssim Re_b \lesssim 200$, for which isotropy is an issue. By contrast, some of the most intense turbulence occurs in the equatorial undercurrent in the central Pacific. Examining overturns

between the base of the surface mixed layer and 350 m, Peters et al. (1995) found buoyancy Reynolds numbers of $20 \lesssim Re_b \lesssim 10^5$ and Froude numbers of $0.2 \lesssim Fr \equiv u_{rms}/Nl_{rms} \lesssim 3$ (**Figure 1*b***). Consequently, simulations of pycnocline mixing should include $Re_b \leq 200$ to address background conditions and need not exceed $Re_b \approx 10^5$ to address most of the more energetic regions.

$k = 0.4$: von Kármán's constant

6. OCEAN MEASUREMENTS

The mixing coefficient $\gamma_{\chi\epsilon}$ has been estimated in many regimes, but the only ensemble of $\hat{R}_f$ estimates came from a tidal channel, and only a few rough estimates of R_f have been reported, based on short horizontal transects.

6.1. Direct Measurements of the Buoyancy Flux

The most direct measurements of vertical heat fluxes came from thermistors and triaxial clusters of small current meters beneath ice floes (Smith 1974, McPhee 1992). Yamazaki & Osborn (1990, 1993) measured the vertical heat flux on the bow of a research submarine using thermistors and airfoils sensing $w'(x_1)$ and $u_2'(x_1)$ and indicating axial symmetry with $\epsilon_a = \nu[5\overline{(\partial u_2'/\partial x_1)^2} + 2.5\overline{(\partial w'/\partial x_1)^2}]$. Comparing direct fluxes, $\overline{w'T'}$, with estimates using the method of Osborn & Cox (1972) required $\gamma_{R_f} = 0.05$. The same approach to data from a 3.8-m-long towed body yielded $R_f \leq 0.25$ (Fleury & Lueck 1994).

Lacking measurements of turbulent production, Holleman et al. (2016) estimated $\hat{R}_f$ with ϵ from linear fits to the $k^{-5/3}$ inertial subrange of velocity spectra from a 1,200-kHz acoustic Doppler current profiler on the bottom. The turbulence was often intense, with ϵ up to 10^{-3} W kg^{-1}. Fitting the viscous-convective subrange of small-scale electrical conductivity from along-channel sections yielded χ_S and $J_b \approx g\beta\chi_S/(2\partial\overline{S_A}/\partial z)$ in the salinity-dominated profiles. During ebb tide, $\hat{R}_f$ rose from ≈0.2 to ≈0.25 before dropping to 0.15 (**Figure 2**). There was considerable scatter, with peak values similar to those in grid wakes (Rohr et al. 1984). $\hat{R}_f$ had two classes, buoyancy limited, with overturns close to the Ozmidov scale, l_O, and bottom limited. The former had $\overline{\hat{R}_f} = 0.23 \pm 0.23$ with no significant trend versus Re_b (**Figure 2**). Boundary-limited samples, with $l_O/kz > 1/4$, decreased with increasing Re_b and had $\overline{\hat{R}_f} = 0.17 \pm 0.02$ (**Figure 2**). Lower efficiency close to the bottom resembles the R_f decreases found in simulations of convecting layers following Monin-Obukhov scaling (Scotti & White 2016).

6.2. Estimating $\gamma_{\chi\epsilon}$

The observations in **Table 4** derive from direct ϵ and χ_T measurements. (Indirect ϵ estimates from the diffusive roll-off of temperature gradient spectra add additional uncertainty and are not considered here.) Aside from very low values in fish aggregations and 0.58 in a tidal channel, $\gamma_{\chi\epsilon}$ is mostly between 0.1 and 0.3, i.e., not far from 0.2, but with considerable scatter. The scatter is not surprising in view of the effect on efficiency of variations in K_S/K_T (Section 2.5).

6.2.1. Variation with Re_b. Velocity and temperature microstructure on the equator at 140°W yielded $\overline{\gamma_{\chi\epsilon}} = 0.12$ with no trend over $1 \lesssim Re_b \lesssim 2 \times 10^5$ (**Figure 3**). Subsequent measurements at the same site that also resolved fine-scale velocity to 0.1 m (**Figure 1**) permitted comparison against the Reynolds number, finding $\gamma_{\chi\epsilon}$ increasing weakly for $200 \lesssim Re \lesssim 10^4$ (Peters et al. 1995). Reexamining NATRE microstructure, Ruddick et al. (1997) used only microscale shear and strain spectra consistent with universal turbulent spectra. When uncertainty in background

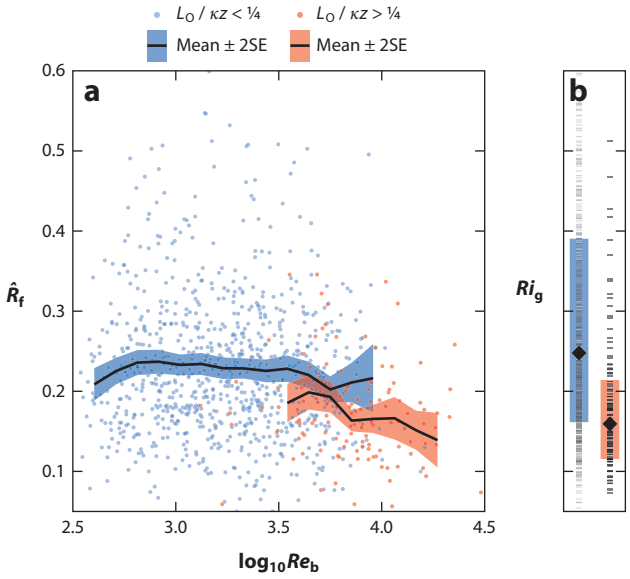

Figure 2

(*a*) $\hat{R}_f$ in the Connecticut River versus $\log_{10} Re_b$. Buoyancy-limited samples are blue, and bottom-limited ones are red. (*b*) Gradient Richardson number, Ri_g. L_O is the Ozmidov scale, and shading shows 95% confidence limits. Adapted from Holleman et al. (2016).

temperature gradients was less than 25%, $\gamma_{\chi\epsilon}$ increased from ≈0.1 at $Re_b = 40$ to ≈0.35 at $Re_b \approx 200$ (**Figure 4**).

6.2.2. Salt fingering during the North Atlantic Tracer Release Experiment. Reanalysis of NATRE profiles found evidence (e.g., tilted shadowgraph images) for fingering where $Ri_g > 1$ and $1 < R_\rho < 2$ (St. Laurent & Schmitt 1999). Where fingering was most favorable, ($1 < R_\rho < 1.6$), efficiency was somewhat higher ($0.2 < \gamma_{\chi\epsilon} < 0.3$) than it was where turbulence was dominant ($0.1 < \gamma_{\chi\epsilon} < 0.3$). As part of their NATRE reanalysis, Ruddick et al. (1997) saw a statistically significant decreasing trend for $\gamma_{\chi\epsilon}$ when $1.5 < R_\rho - 1 < 4$ (**Figure 5**). At lower R_ρ, $\gamma_{\chi\epsilon}$ was roughly consistent with salt fingering, but Monte Carlo simulations suggested noise contamination. This analysis, however, depends on the implicit assumption by Oakey (1982) that $K_S = K_T$ during turbulent mixing (Section 2.5) and needs to be reexamined for the possibility of differential diffusion, e.g., in the decrease of $\gamma_{\chi\epsilon}$ with increasing R_ρ in **Figure 5**.

6.3. Summary of Observational Estimates

Most observations find $0.1 \lesssim \gamma_{\chi\epsilon} \lesssim 0.3$, but overall, there is no observational basis for not using $\gamma_{\chi\epsilon} = 0.2$; some ensembles differ and have tight error bars, but there is no consistency from one set to the next. Owing to many possible sources for biases and errors, this is not surprising for the ratio of two partially correlated lognormal variables, e.g., in **Figure 3**. Differences may also reflect dependencies on unreported background parameters: N^2, Ri_g (or Fr), R_ρ, and Re (or Re_b). In spite of the uncertainties, the observations are not consistent with the mixing coefficient decreasing significantly for $Re_b \gtrsim 100$, as found in some laboratory and numerical results (Sections 7 and 8). Evidence for salt fingering is intriguing, and the possibility should be considered during future measurements. Conclusive evidence, however, will require direct χ_S measurements. One caveat is

Table 4 $\gamma_{\chi\epsilon}$ in pycnoclines from direct χ_T and ϵ measurements, mostly by profiling

Location	R_ρ	Re_b	$\gamma_{\chi\epsilon}$	Reference
Rockall Trough	>7	300–3,000	0.05–0.32	Oakey 1982, 1985[a]
California Current	Variable	—	0.18[b]	Gregg et al. 1986
Equator, 140°W[c]	Variable	1–10^6	0.12[b]	Peters & Gregg 1988
Equator, 140°W[c]	—	—	0.12–0.48[d]	Moum et al. 1989
California Current	—	—	0.05[e]	Yamazaki & Osborn 1993
Admiralty Inlet	−0.05	$\approx 3 \times 10^4$	0.58[f]	Seim & Gregg 1994
Tidal channel	—	—	0.25, 0.23[g]	Gargett & Moum 1995
Equator, 140°W[h]	—	20–10^5	0.14[h]	Peters et al. 1995
Northeast Pacific	—	—	≈0.3–0.4	Moum 1996
Northeast Atlantic	−0.8 to 5	30–4,000	0.14, 0.21[i]	Ruddick et al. 1997
Northeast Atlantic[j]	−100 to −1	—	0.16 ± 0.04	St. Laurent & Schmitt 1999
	>1	—	0.2–0.3	
Monterey shelf[k]	—	—	0.0022	Gregg & Horne 2009
Equator, 80.5°E[k]	—	—	<0.02	Pujiana et al. 2015

Abbreviation: —, not reported.
[a]Reanalysis of Oakey's data by Ruddick et al. (1997).
[b]Arithmetic mean.
[c]10–140 m in the equatorial undercurrent.
[d]In 83 selected overturns.
[e]From a submarine.
[f]Average over large overturns with $0.17 < \gamma_{\chi\epsilon} \leq 1.3$, χ_T multiplied by $(1 + 1/R_\rho^2)$ to account for salt stratification.
[g]For positive and negative density fluxes.
[h]Median from 0 to 350 m, through the undercurrent.
[i]Fall and spring, ±0.02 confidence.
[j]North Atlantic Tracer Release Experiment (NATRE) reanalysis and Pacific seamount. The values in the first row are from turbulent sections; those in the second row are from salt-fingering regions.
[k]In fish aggregations.

that these conclusions are based on intensive measurements and tracer releases in the upper ocean and may need modification after further abyssal observations.

7. LABORATORY EXPERIMENTS

Among the laboratory techniques for generating mixing in stratified water (**Table 5**), the simplest oscillate grids or paddles. Some use baffles to recirculate stratified flow through a grid, and yet others generate KH shear instabilities by temporarily tilting a long, thin tank containing two layers separating a stratified interface. How accurately these techniques simulate internal wave breaking in the pycnocline remains uncertain (Section 5).

Laboratory experiments and ocean measurements also differ in how mixing is measured and efficiency defined. Changes in stratification and potential energy can be measured easily in tanks, leading to $\mathcal{E}_{pe1}$ and $\mathcal{E}_{pe2}$. However, there have been no estimates of ΔPE in the pycnocline, owing to the difficulty of observing the full temporal and spatial evolution of mixing events. On the other hand, ϵ and χ_T, which are easily measured in the ocean, often involve scales too small to measure in tanks. For example, unable to measure ϵ directly, McEwan (1983b) estimated it from the rate of working by his paddle. Consequently, mixing efficiencies and coefficients are

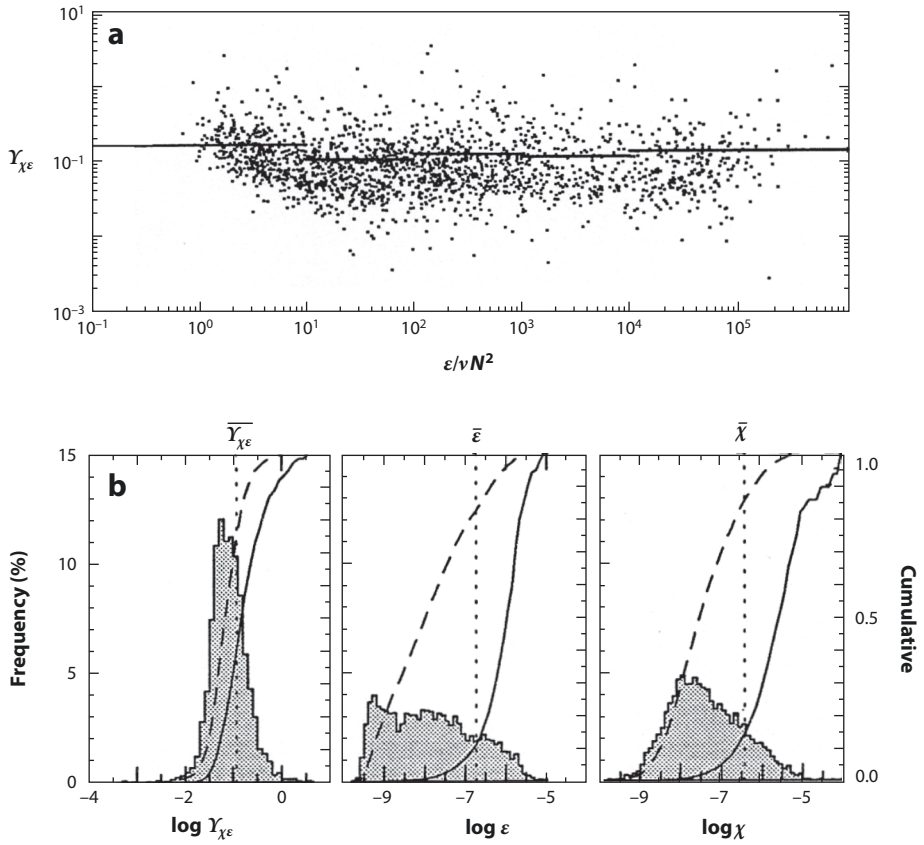

Figure 3

(*a*) Hourly means of $\gamma_{\chi\epsilon}$, ϵ, and χ_T over $\Delta z = 6.4$ m from 23 to 144 m at the equator at 140°W, showing no trend for $1 \leq Re_b \leq 2 \times 10^5$. (*b*) The $\gamma_{\chi\epsilon}$ distribution, which is nearly lognormal and much narrower than the ϵ and χ_T distributions. Adapted from Peters & Gregg (1988).

Table 5 Laboratory experiments examining mixing efficiency and mixing coefficients

Technique	Results	Reference
Vertically oscillating grid	K_T, K_S	Turner 1968
Tilt tank shear flow	$\Delta PE/\Delta KE$	Thorpe 1973
Oscillating paddle generating internal waves	$\Delta PE/\epsilon$	McEwan 1983b
Recirculating grid flow	R_f	Rohr et al. 1984
Reanalysis of laboratory data from Van Atta and colleagues (e.g., Rohr et al. 1984)	R_f	Ivey & Imberger 1991
Horizontally oscillating grid	K_ρ	Barry et al. 2001
Recirculating shear flow	R_f	Strang & Fernando 2001
Vertical combs stirring tank	R_f, K_T, K_S	Jackson & Rehmann 2003

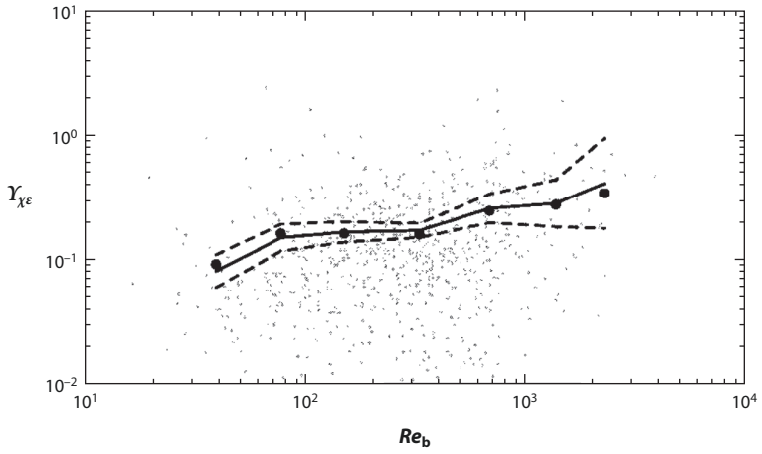

Figure 4

$\gamma_{\chi\epsilon}$ versus Re_b from 738 samples during the North Atlantic Tracer Release Experiment (NATRE). The solid line connects arithmetic means, and the dashed lines are 95% confidence limits. Adapted from Ruddick et al. (1997).

defined and measured differently for laboratory and numerical studies than for ocean observations, complicating comparisons.

To examine mixing by KH instabilities, Thorpe (1973) tilted a long, thin tank with two-layer stratification and profiled with a single-needle conductivity probe and a hot-film velocity sensor. Computing $\mathcal{E}_{pe}$ demonstrated a steady decrease in efficiency as the Richardson number increased, from 0.212 at $Ri_g = 0.06$ to 0.098 at $Ri_g = 0.14$.

McEwan (1983b) compared density profiles before and after paddle-induced mixing to estimate the increase in the height of the center of mass, δz, leading to $\mathcal{E}_{pe} = (g\,Q\delta z)/[P(E-V)/E]$, where

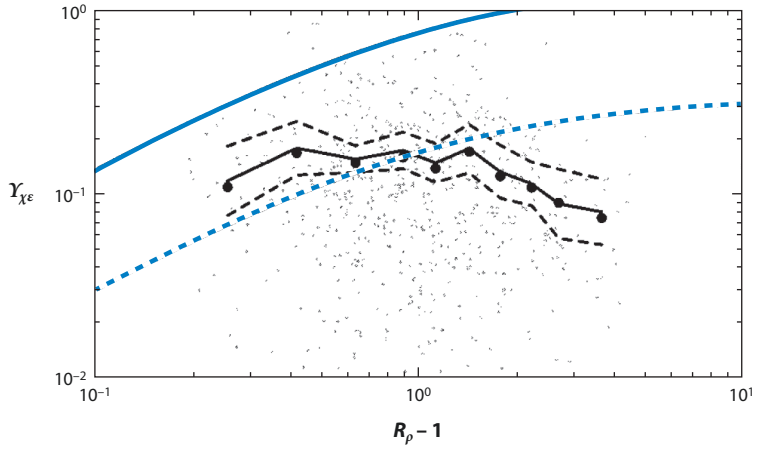

Figure 5

$\gamma_{\chi\epsilon}$ with the mean (*solid line*) and 95% confidence limits (*dashed lines*) versus R_ρ. The blue solid and dashed lines are mixing coefficients expected for salt fingering with flux ratios, R_{flux}^{sf}, of 0.6 and 0.25, respectively. Adapted from Ruddick et al. (1997).

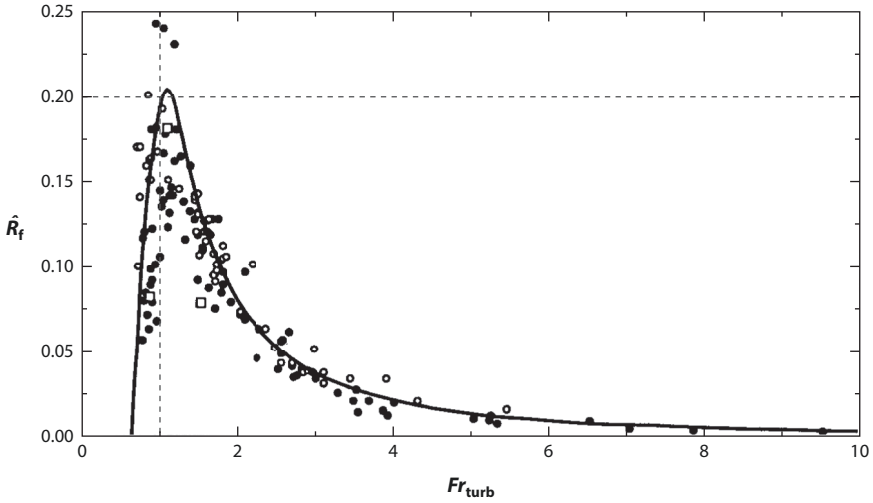

Figure 6

$\hat{R}_f$ versus the turbulent Froude number, Fr_{turb}, using laboratory data from Van Atta and colleagues (e.g., Rohr et al. 1984). Adapted from Ivey & Imberger (1991).

Q is the fluid mass, P is the total energy input, V is the power dissipated by laminar viscosity, and E is proportional to the net forcing power per unit mass. Efficiency ranged from 0.15 to 0.36 and averaged 0.26 ± 0.06 (1 standard deviation) as Re_b varied from 2.9 to 14.1 and averaged 6.3.

7.1. Variation of $\hat{R}_f$ with Fr

Reanalyzing laboratory data from Van Atta and colleagues (e.g., Rohr et al. 1984), Ivey & Imberger (1991) normalized the density flux as $R_{\rho w} \equiv (\overline{\rho' w'})/(\rho_{rms} w_{rms})$ to obtain $\hat{R}_f = 1/(1 + Fr_{turb}^2/R_{\rho w})$. [Having only ϵ and the centered displacement scale, L_C, the Froude number was estimated as $Fr_{turb} \equiv (\epsilon/N^3 L_C^2)^{1/3}$.] Rising abruptly to 0.2 as Fr approaches 1 from below, $\hat{R}_f$ decreases gradually as Fr exceeds 1 (**Figure 6**). The authors allowed that some of the scatter may result from variations in Re.

7.2. Variation of K_ρ with Re_b

Barry et al. (2001) used a horizontally oscillating vertical grid to stir stratification that was initially linear in the bottom 80% of the tank. As mixing proceeded, the relatively well-mixed top layer thickened and another mixed layer grew from the bottom until most of the tank was homogeneous during the last runs (**Figure 7*a***). After a stirring run lasting Δt seconds, mixing was expressed as $K_\rho = \Delta GPE_r/Vg\Delta t(d\rho/dz)_{avg}$, where V is the tank volume. Average dissipation was $\int \rho\epsilon \, dV = \sigma_{grid} \times F_{drag} \times u_{grid}/\Delta t$, where σ_{grid} is the fraction of the grid that was solid. Composite results show $K_\rho \propto Re_b$ up to $Re_b \sim 300$, but the magnitude is about half that expected using the method of Osborn (1980) (**Figure 7*b***). For larger Re_b, the dependence changes to $K_\rho \propto Re_b^{1/3}$.

We question the applicability of these results to ocean mixing, in part because a significant fraction of energy input by a vertical grid oscillating horizontally is likely to be dissipated against tank walls without doing any mixing. Also, presuming that the stirring intensity remained constant, it is likely that the primary difference between small and large Re_b resulted from N^2 decreasing as

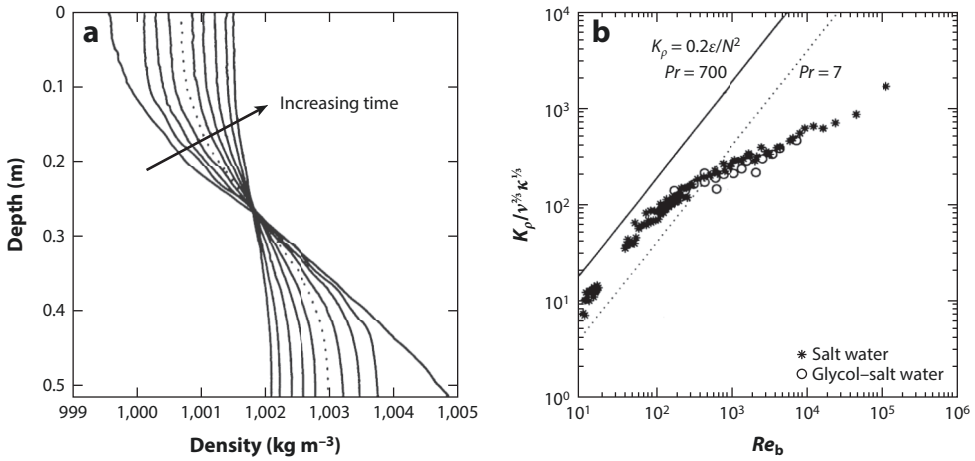

Figure 7

(*a*) Density evolution during grid stirring. (*b*) K_ρ normalized by $\nu^{2/3}\kappa_S^{1/3}$ to incorporate measurements in a salt water tank and in a glycol–salt water tank. The Re_b slope changes from 1:1 to 1:3 at $Re_b \sim 300$. Solid and dotted lines show $K_\rho/\nu^{2/3}\kappa^{1/3} = 0.2\epsilon/N^2$ for $Pr = 700$ (salt water) and $Pr = 7$ (thermally stratified water). Adapted from Barry et al. (2001).

the tank was homogenized. Moreover, thickening of the upper and lower boundary layers would have absorbed a growing fraction of the dissipation without significantly altering density. As a minimum, N^2 and Ri_g should be considered as additional parameters to interpret the observations.

7.3. Summary of Laboratory Experiments

Laboratory experiments clearly show that mixing efficiencies can span a wide range of values, with maxima near 0.2 and minima of zero in homogeneous fluids. In most cases, Re_b was small; the exception was the results of Barry et al. (2001), who found efficiency decreasing significantly when $Re_b \gtrsim 100$. We question this finding because horizontal stirring would have produced significant dissipation at the tank walls, and decreasing efficiency was found when profiles were nearly homogeneous. We consider laboratory examination of differential diffusion along with numerical simulations in Section 8.5.

8. NUMERICAL SIMULATIONS

Most numerical simulations are direct, resolving lengths from the event down to the Kolmogorov scale, l_η, when $Pr = 1$ or to the Batchelor scale, l_κ, when $Pr > 1$. The bandwidth for a spectrally accurate method is from 1 to $N/2$, where wave number 1 corresponds to the domain size for an N-point numerical grid. Thus, the maximum spectral bandwidth is $N/2M$ for an event occupying $1/M$ of the domain; e.g., when $N = 128$ and $M = 2$ (half of the domain), the maximum spectral bandwidth is 32 (**Table 6**). Lower-order numerical methods have typical bandwidths closer to $N/4M$. Bandwidths this small greatly restrict available Reynolds numbers, $Re \sim (l_e/l_\eta)^{4/3}$, where l_e is the integral scale (Pope 2000). Inadequate spatial resolution is a serious issue except for the most recent simulations and gets worse when $Pr > 1$, as the number of grid points needed increases as $\sqrt{Pr}$. Because the Schmidt number, Sc, in the ocean is 500–3,000, the resolution problem is

l_η: $\left(\frac{\nu^3}{\epsilon}\right)^{1/4}$

l_κ: $l_\eta \left(\frac{\nu}{\kappa}\right)^{1/2}$

Table 6 Selected numerical simulations addressing mixing efficiency, most of which are direct numerical simulations

Mode	*Pr*	*Sc*	*Re*	Ri_g	Grid[a]	Reference
IW	1	—	300–10^6	—	128 × 64 × 128	Lombard & Riley 1996b
Shear	—	—	—	0.04–0.17	—	Jacobitz et al. 1997
IW[b]	—	—	—	—	256 × 256 × 64	Lelong & Dunkerton 1998a,b
KH	1	—	—	0–0.1	100 × 100 × 100	Caulfield & Peltier 2000
KH	0.7–1.4	—	—	0.041–1.4	128 × 128 × 257	Staquet 2000
KH	1–7	—	701–4,978	—	512 × 64 × 256	Smyth et al. 2001
IW[c]	0.72	—	5,400	603[d]	256 × 256 × 256	Bouruet-Aubertot et al. 2001
Holmboe	9	—	1,200	—	256 × 128 × 128	Smyth & Winters 2003
Interface	7	—	2,179	—	128 × 128 × 128	Fringer & Street 2003
Vortices	1	—	800–6,400	—	512 × 512 × 512	Riley & de Bruyn Kops 2003
KH	0.72	—	89.4[e]	0.04–1.0	128 × 128 × 128	Shih et al. 2005
KH	7	50	100–300	0.01–0.12	512 × 128 × 192	Smyth et al. 2005
Mode 1	7	70	—	—	256 × 256 × 256	Merryfield 2005
Shear	0.2–5	—	640–3,200	0–0.1	256 × 128 × 768	Brucker & Sarkar 2007
Holmboe	9	—	1,200–2,400	0.15–1.0	128 × 64 × 128	Smyth et al. 2007
KH	1	—	1,280	0.1	384 × 128 × 512	Pham et al. 2009
KH	1	—	5,000	0.1	1,024 × 512 × 768	Pham & Sarkar 2010
KH	1	—	750–8,000	0.01–0.20	1,024 × 128 × 1,216	Mashayek & Peltier 2011
KH	1	—	6,000	0.05–0.20	1,280 × 256 × 1,216	Mashayek et al. 2013
KH	1–16	—	6,000	0.12–0.20	1,800 × 180 × 880	Salehipour et al. 2015
KH	1–16	—	6,000–12,000	0.12	1,800 × 360 × 1,560	Salehipour & Peltier 2015
Forced	1	—	178–220	—	4,096 × 8,192 × 8,192	de Bruyn Kops 2015
Forced	1	—	120–43,180	—	4,096 × 4,096 × 1,024	Maffioli et al. 2016
Holmboe	8	—	100–6,000	0.16	1,450 × 260 × 1,160	Salehipour et al. 2016

Abbreviations: IW, internal waves; KH, Kelvin-Helmholtz; —, not applicable.
[a]Grid ($N_x \times N_y \times N_z$) gives the largest grid size.
[b]The model uses a hyperviscous operator.
[c]All characteristics are for the three-dimensional propagating wave.
[d]$Ri_g = Fr^{-2}$.
[e]Taylor microscale Reynolds number.

extreme when simulating differential diffusion. Consequently, most simulations have estimated efficiency for $Pr = 1$, and only two also had $Sc \gtrsim 50$.

Most studies examined the instability of a sheared density interface. When stratification and shear interfaces approximately coincide, instabilities take the KH form, but when the velocity interface is significantly thicker, Holmboe instabilities develop (Smyth & Winters 2003). Most studies have focused on KH, applying increasing numbers of grid points to examine their evolution as functions of *Pr*, Ri_g, and *Re*. Some simulations, however, address the nature of mixing produced by breaking internal waves (e.g., for a review of earlier work, see Riley & Lelong 2000). Because internal waves of any amplitude propagating in a uniform environment with no background subinertial shear are unstable to both two- and three-dimensional disturbances, their breakdown cannot generally be classified as either shear driven or convectively driven (Mied 1976, Drazin 1977, Lombard & Riley 1996a).

8.1. Interface Thickness: Kelvin-Helmholtz Versus Holmboe Instabilities

Fringer & Street (2003) studied the effect of interface thickness, δ, relative to the wavelength, k, and amplitude of standing and progressive internal waves on interfaces. Instabilities develop when $k\delta < 0.56$, but they lack the energy to form the two-dimensional convective instabilities necessary for strong turbulence. Instabilities with $0.56 < k\delta < 2.33$ and $Ri_0 < 0.13$ generate vigorous secondary convective instabilities and turbulence, mixing most effectively when $k\delta = 1$. Internal waves with $k\delta > 2.33$ are too thick to form KH billows and instead produce convective, or Rayleigh-Taylor, billows. Smyth & Winters (2003) found Holmboe waves as primary instabilities on interfaces that have velocity length scales more than 2.4 times the density length scales and as secondary instabilities on KH instabilities that had grown large.

8.2. Kelvin-Helmholtz Instabilities

Because Kelvin-Helmholtz instabilities are assumed to be the dominant mechanism mixing the ocean pycnocline and the problem is well posed, extensive modeling has sought to understand how these events evolve as functions of key parameters. As computer capacity has improved, some models used realistic Prandtl numbers, and a few also included Schmidt numbers significantly larger than the Prandtl numbers but still smaller than those in the ocean. Gradient Richardson numbers or Froude numbers have also been varied, as have Reynolds numbers.

8.2.1. Evolution. KH instabilities develop when Ri_g is significantly below 1/4 and small perturbations grow to generate spanwise vortices, or billows. Horizontal wavelengths are typically 6–11 times the interface thickness (Smyth & Moum 2012). Initial growth is two dimensional, confining kinetic energy to vertical and streamwise velocities. When the initial Reynolds number, Re_0, is small or moderate, billows grow by pairing until they are suppressed by stratification. Within gravitationally unstable regions of the core, shear-aligned convective secondary instabilities produce small streamwise vortices that rapidly transition to turbulence. Dissipation-scale velocity is nearly isotropic after the transition (shaded on the top axis of **Figure 8*a***), but as decay proceeds, vertical and spanwise components are increasingly weaker than streamwise flow. With increasing Re_0, additional secondary instabilities develop, preventing vortex pairing (Mashayek & Peltier 2011, Salehipour et al. 2015). These, however, do not significantly change efficiency.

Smyth et al. (2001) studied KH mixing efficiency for $Pr = 1$–7, $Ri_0 = 0.08$–0.16, and $Re_0 = 701$–$4{,}978$ using a grid resolution about five times the smallest Batchelor scale. Dissipation rates, ϵ and χ_T, were computed directly from the strain tensor and resolved temperature gradients. APE increased rapidly as the billows grew, whereas GPE_r started growing later as extensional straining greatly thinned the interface, also known as braids, between adjacent billows (**Figure 8**). $dGPE_r/dt$ peaked when stratification inhibited further growth of the billows, and maximum ϵ followed shortly after the transition to turbulence. Turbulent production and dissipation often differed wildly and balanced only when averaged over events. Owing to the lag between $dGPE_r/dt$ and ϵ, mixing efficiency, $\mathcal{E}_{pe2}$, rose rapidly to near unity before declining irregularly to $\approx$0.2. Subsequent studies found that forcing governs cumulative mixing efficiency by altering the duration and intensity of preturbulent and turbulent diffusion (Inoue & Smyth 2009), suggesting that cumulative efficiency should be reported when possible.

As KH instabilities evolve, the ratio of the Ozmidov to the Thorpe scale increases with instability age (Dillon 1982, Wijesekera & Dillon 1997). Smyth et al. (2001) expressed mixing efficiency

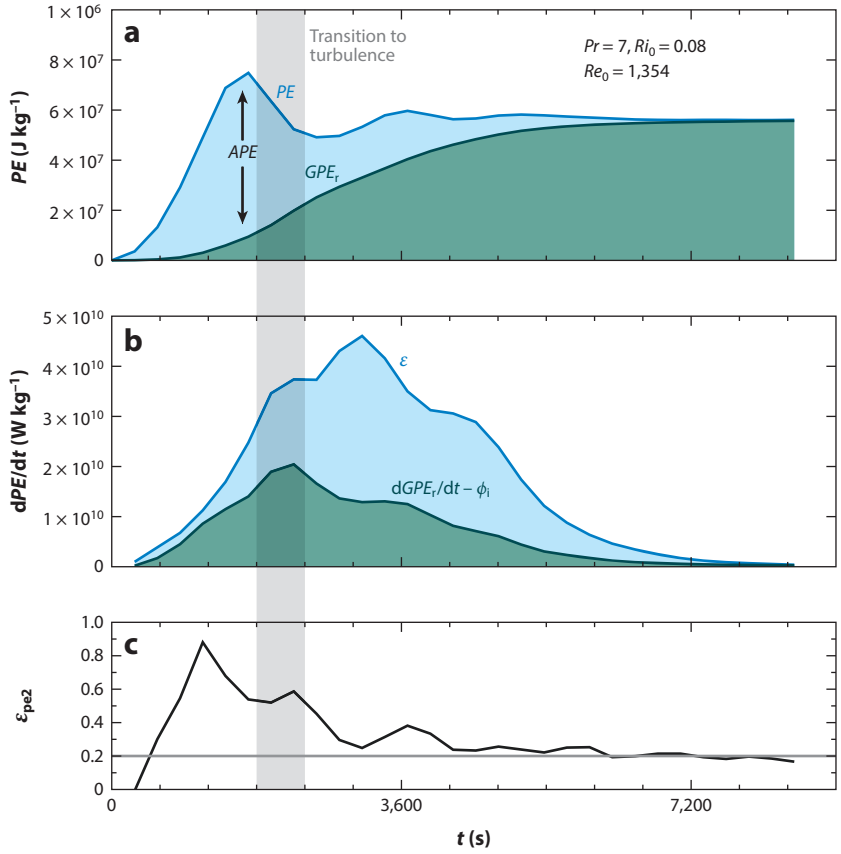

Figure 8

Direct numerical simulation of a Kelvin-Helmholtz instability, showing (*a*) total and background potential energy (*PE*), (*b*) domain averages of dissipation and the time derivative of background *PE*, and (*c*) $\mathcal{E}_{pe2}$. The shading shows when the transition to turbulence occurs; the gray line in panel *c* indicates the standard efficiency of 0.2. Adapted from Smyth et al. (2001).

in terms of this age as

$$\mathcal{E}_{pe2} \approx 0.33\,\hat{R}_{OT}^{-0.63}, \quad \text{where} \quad \hat{R}_{OT} \equiv \frac{l_O}{l_e^{3/4} l_{th}^{1/4}} \qquad 12.$$

is a weighted length scale ratio and l_e is the root-mean-square temperature fluctuation divided by the average temperature gradient. Using $\hat{R}_{OT}$ as a clock is promising, but further work is needed, including simulations at higher Reynolds numbers, before this approach should be routinely applied to observations (W. Smyth, personal communication).

8.2.2. Prandtl number influence. Scalar diffusion increases more rapidly than viscous dissipation during KH roll-up because strain in preturbulent billows evolves at a rate close to optimal for mixing owing to the alignment of density gradients (W. Smyth, personal communication). Consequently, $\gamma_{\chi\epsilon}$ initially becomes very large (Winters et al. 1995, Smyth et al. 2001). Runs with increasing Prandtl numbers demonstrate that the mixing coefficient decreases during the most active phase of the instability as molecular diffusivity decreases. Averaging seven simulations, Smyth

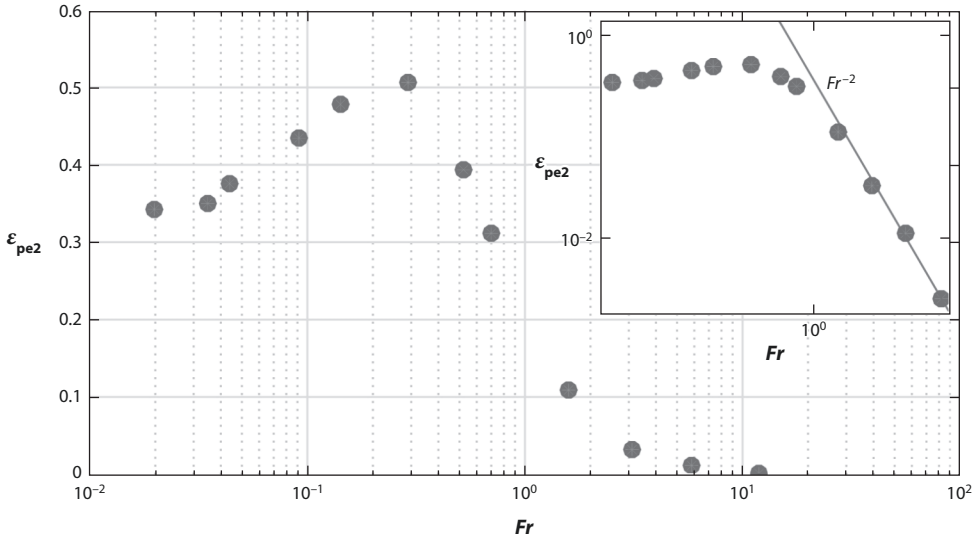

Figure 9

$\mathcal{E}_{pe2}$ versus $Fr \equiv \epsilon/(N u^2)$ for microscale Reynolds number $Re_\lambda > 200$. Adapted from Maffioli et al. (2016).

et al. (2001) found R_f decreasing from ≈0.35 to ≈0.22 as Pr increased from 1 to 7. Varying the Prandtl number demonstrates that molecular diffusion has a profound effect on the sequence of secondary instabilities developing at higher Reynolds numbers (Salehipour et al. 2015). The net effect decreases $\mathcal{E}_i$ and $\mathcal{E}_c$ from ≈0.24 at $Pr = 1$ to ≈0.18 at $Pr = 16$.

8.2.3. Richardson and Froude number influence. Maffioli et al. (2016) suggested that when $Pr = 1$ and Re_b is high enough, $\mathcal{E}_{pe}$ should become independent of Re_b and depend only on large Froude numbers as

$$\mathcal{E}_{pe2} \propto \frac{N^2 u l}{u^3/l} = \frac{N^2 l^2}{u^2} = Fr^{-2}, \qquad 13.$$

where the length scale is assumed to be horizontal. That is, they expressed Taylor scaling as $l = l_h \sim u'^3/\epsilon$. At low Froude numbers, $l_h \gg l_v$, and $\mathcal{E}_{pe}$ should asymptote to a constant (**Figure 9**). Direct numerical simulations of forced turbulence in stratified profiles were consistent with the predicted behavior, with $\mathcal{E}_{pe2}$ approaching 0.34 for $Fr \ll 1$, rising to about 0.5 at $Fr = 0.3$ and then decreasing as Fr^{-2} (**Figure 9**). Their results at low Froude numbers, however, require verification, as different forcing mechanisms and lower Re_b were required to obtain them.

Similar simulations at somewhat higher resolution by de Bruyn Kops (2015) supported Maffioli et al.'s (2016) conclusion that ϵ_{pe2} should decrease at lower Fr. At fixed Fr, however, as Re_b decreased from 200 to 14, ϵ_{pe2} decreased by about 30%. Repeating these simulations for $Pr = 7$ at appropriately higher resolution (13,104 × 13,104 × 6,552), de Bruyn Kops (personal communication) found ϵ_{pe2} decreasing somewhat with the increase in Pr, qualitatively similar to the results of Smyth et al. (2001) and Salehipour et al. (2015).

8.2.4. Reynolds number influence. When overturns match the Ozmidov scale, l_O, turbulence is limited by stratification, and Re_b is similar to Re but not necessarily equal (Section 4). Because this condition is common in the ocean, turbulent parameters are often examined as functions of Re_b,

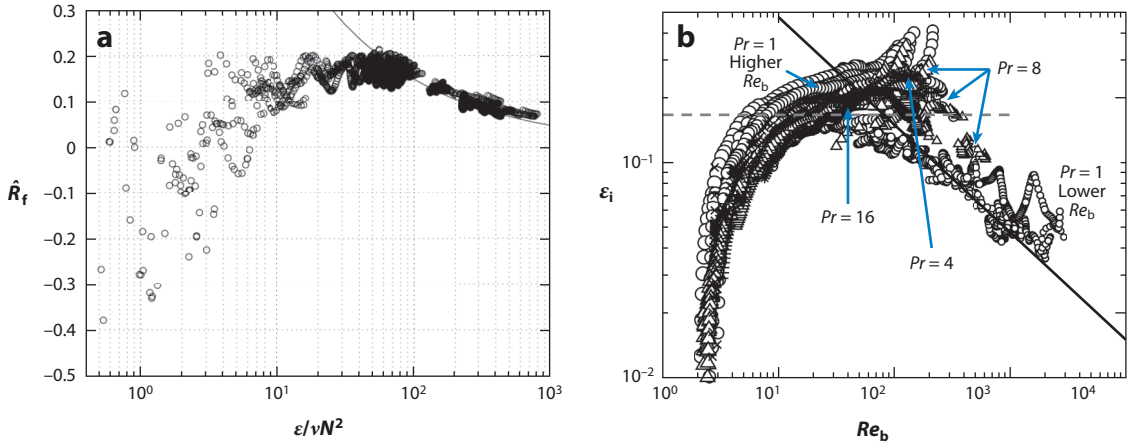

Figure 10

(*a*) $\hat{R}_f$ versus $Re_b \equiv \epsilon/\nu N^2$ from direct numerical simulation of Kelvin-Helmholtz instabilities (Shih et al. 2005). Countergradient fluxes are included in the curve $Re_f = 1.5 Re_b^{-1/2}$. (*b*) Instantaneous mixing efficiency from direct numerical simulation of Kelvin-Helmholtz instabilities versus Re_b. A convincing break in slope occurs only for $Pr = 1$. Adapted from Salehipour & Peltier (2015).

which can be estimated from measurements of ϵ and N^2 in lieu of energy-containing velocities. As noted above, however, comparing parameters versus only Re_b is problematic if N varies widely, particularly when stratification is very weak.

Two sets of direct numerical simulations found $\hat{R}_f$ and $\mathcal{E}_i$ decreasing at high Re_b (**Figure 10**). Specifically, Shih et al. (2005) found that Equation 11 is valid only when $7 < Re_b < 100$, transitional between nearly laminar diffusion and energetic turbulence, both of which mix less efficiently. Using a $128 \times 128 \times 128$ grid, Shih et al. (2005) resolved a wave-number bandwidth of only 32 if the largest scales filled half of the domain. Consequently, Kunze (2011), Kunze et al. (2012), and Mater & Venayagamoorthy (2014) suggested that the efficiency decrease may have been an artifact of inadequate spatial resolution. Alternatively, if the largest scales filled more than half of the domain, the reduced efficiency may indicate boundary influence (Holleman et al. 2016, Scotti & White 2016). Salehipour & Peltier (2015) also found decreasing efficiency as the number of grid points increased, but only runs with $Pr = 1$ extended sufficiently past $Re_b = 100$ to demonstrate a convincing decrease, and in these cases N was very small.

While maintaining Pr and the initial gradient Richardson number, Ri_0, Mashayek & Peltier (2013) did not find KH efficiency decreasing as Re increased to 6,000; all four runs had the same initial rise to $\mathcal{E}_i > 0.7$ followed by rapid decay (**Figure 11**). During the decay, runs with $Re =$ 4,000 and 6,000 fell more slowly and settled closer to $\mathcal{E}_i = 0.3$ than to $\mathcal{E}_i = 0.2$.

8.3. Holmboe Instabilities

Holmboe instabilities develop elliptical vortices above and below density interfaces that scour and displace the interfaces to form periodic cusps. Simulations with velocity interfaces three times thicker than density interfaces found mixing from the sharpened laminar gradients increasing as the initial Richardson number, Ri_0, rose from 0.3 to 1.0 (Smyth et al. 2007). By delaying the transition to turbulence, net mixing grew as stratification increased. When Ri_0 was reduced to 0.15, however, KH instabilities developed that mixed much more strongly than any of the Holmboe

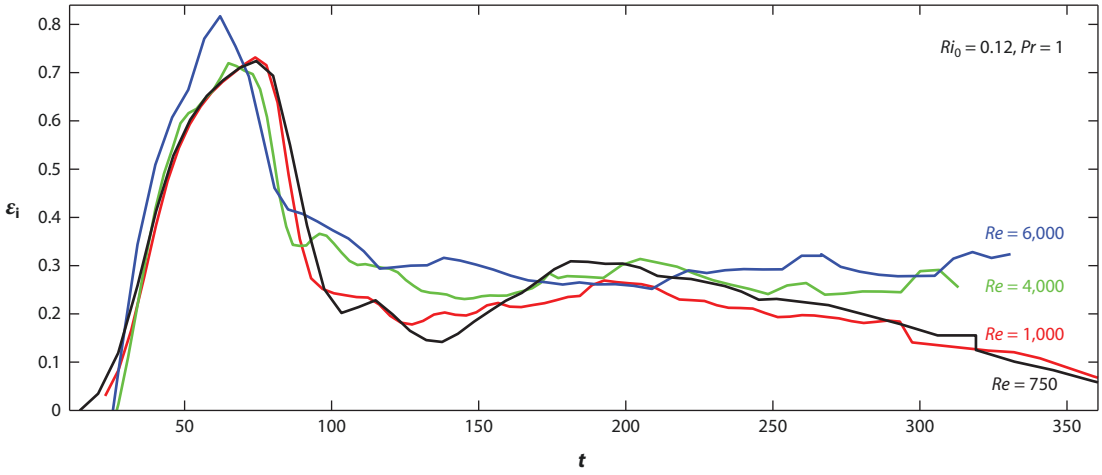

Figure 11

Instantaneous mixing efficiency during direct numerical simulation of Kelvin-Helmholtz instabilities. Time is scaled by $(\delta/2)/u$, where δ is the interface thickness. Adapted from Mashayek & Peltier (2013).

instabilities. The net increase in potential energy, however, was comparable owing to the longer duration of mixing during the Holmboe instability (**Figure 12**).

In considering velocity and density interfaces offset from each other, Carpenter et al. (2007) found that the degree of asymmetry strongly affects the amount of mixing. As suggested by Salehipour et al. (2016), many other variations remain to be studied.

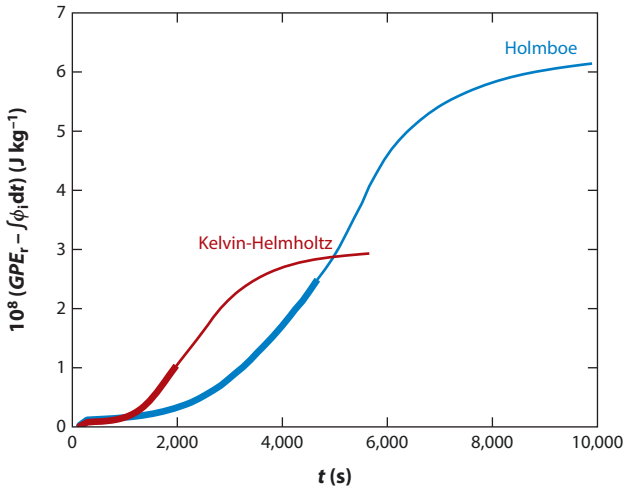

Figure 12

Cumulative potential energy increase by turbulent mixing for Kelvin-Helmholtz and Holmboe instabilities initiated on interfaces of different thickness between the same velocity and density contrasts. The velocity interface triggering the Holmboe instability was thinner than the density interface. Thicker lines mark preturbulent phases of the instabilities. Adapted from Smyth & Winters (2003).

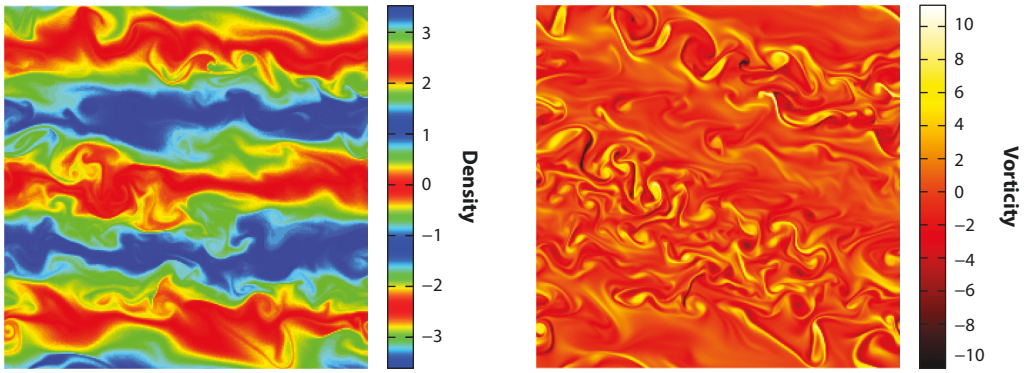

Figure 13

Density and vorticity in the vertical plane after 37.9 buoyancy periods of propagation of a high-frequency ($\omega = N/\sqrt{2}$) internal wave. Adapted from Bouruet-Aubertot et al. (2001).

8.4. Breaking Internal Waves

Following up on analytical studies of internal wave shear instability by Dunkerton (1997), Lelong & Dunkerton (1998a,b) numerically examined how the instability of a single wave varies with frequency and amplitude. At near-inertial frequencies, shear instability dominates and occurs simultaneously throughout the wave field to produce a nearly isotropic spectrum. At intermediate frequencies, shear instability triggers breakdown in the transverse direction when the wave is convectively unstable and diagonally when it is not. As frequencies approach N, convective instability modifies the transverse shear instabilities as they grow to finite amplitude. Thus, waves are susceptible to shear instability before convective overturning begins, except when wave amplitude increases rapidly, e.g., while approaching a critical layer. Lelong & Dunkerton (1998b) speculated that, owing to their global breakdown, near-inertial waves may mix more efficiently than waves with higher frequencies.

Bouruet-Aubertot et al. (2001) investigated propagation and mixing of a high-frequency ($N/\sqrt{2}$) internal wave. Even single internal waves are unstable to triad interactions like the parametric subharmonic instability (PSI) of waves with Garrett & Munk (1975) spectra. Until local overturning began, instabilities grew exponentially at half the wave frequency, forming vorticity bands inclined 20° from horizontal (**Figure 13**). Breaking began in parallel sets of unstable shear layers as the wave lost coherence; the convective instability of the primary wave was inhibited by its shear. During the turbulent phase, $\mathcal{E}_{iw} \approx 0.3$.

8.5. Differential Diffusion

Two studies used direct numerical simulations to examine differential diffusion in profiles stratified by heat and salt, one driven by a first-mode wave (Merryfield 2005) and the other by KH instability (Smyth et al. 2005). Numerical resolution limited Sc to 70 and 50, respectively. These findings and prior results demonstrate that cumulative salt diffusivity is less than half that of heat for weak turbulence, i.e., for $Re_b < 10$ (**Figure 14**). As turbulence becomes more intense, the ratio rises to 1 for $Re_b \geq 100$, according to the simulation and to laboratory measurements with $Re_b \approx$ 300–500 (Jackson & Rehmann 2003). Thus, the range of reduced efficiency includes most of the turbulence produced by background internal waves.

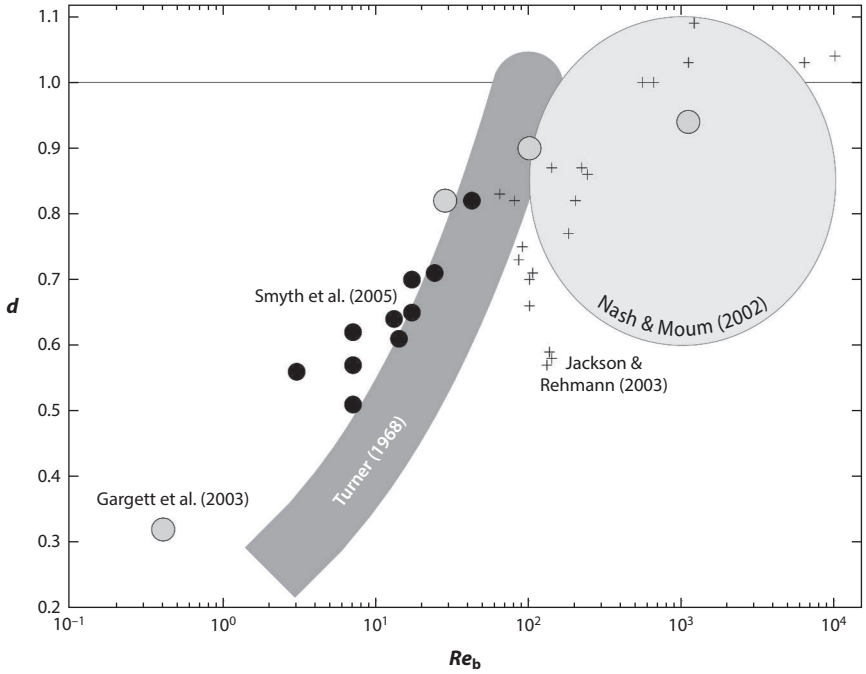

Figure 14

Ratio of the eddy coefficients of salt and heat, $d \equiv \frac{K_{S,c}(t)}{K_{T,c}(t)}$, versus Re_b from the ocean (Nash & Moum 2002), laboratory tanks (Turner 1968, Jackson & Rehmann 2003), and direct numerical simulation (Gargett et al. 2003, Smyth et al. 2005). Adapted from Smyth et al. (2005).

8.6. Summary of Numerical Simulations

Numerical simulations, mostly direct, have explored mixing efficiency in several settings applicable to the ocean, generally as KH instabilities of sheared interfaces bounded by homogeneous layers. The principal findings include the following:

1. Mixing efficiency and mixing coefficients vary with the mechanisms producing the mixing, but the efficiencies of Holmboe and KH instabilities appear to be comparable, as does mixing by breaking internal waves.
2. The efficiency of KH instabilities varies weakly with Pr and strongly with Fr as the latter approaches 1 (Equation 13).
3. Occurring when $K_S \neq K_T$, differential diffusion is significant when $Re_b \lesssim 100$, characteristic of weak mixing found in large parts of the ocean where internal waves are at background.
4. Evidence for systematic variation of efficiency with Re is contradictory. Two studies found efficiency decreasing for $Re_b > 100$, but others showed no change to $Re = 6{,}000$. Decreasing efficiency was found late in the evolution of the instabilities when N^2 was very low, suggesting that efficiency was low because there was little to mix. By contrast, oceanic observations of large Re_b are not confined to weak stratification, a situation models have not been able to replicate and indicating that N^2 should be viewed as an independent parameter.
5. Scaling arguments and results from numerical simulations indicate that the mixing efficiency must depend on at least two parameters, one characterizing the stratification, e.g., Fr or Ri_g, and the other the strength of the turbulence, e.g., Re or Re_b.

9. REDUCTION IN EFFICIENCY DUE TO MIXED-LAYER COLLAPSE

The efficiency analyses above neglect the loss of potential energy as horizontal pressure gradients collapse mixed regions as mixing decays. Comparing potential energy before and after spreading, Garrett (1984) noted that complete spreading would halve the increase accompanying homogenization—say, when a region with thickness h and initial stratification N_0^2 is mixed to have $N^2 = 0$. Hebert (1988) extended the comparison to include partial homogenization N_p^2, obtaining

R_{def}: $\Delta N h/f$, where f is the Coriolis parameter

$$\Delta GPE_{\text{r}} = \frac{\rho_0 h^3 a (N_0^2 - N_p^2)}{24}\left[1 + \frac{a}{A} + \frac{N_p^2}{N_0^2}\left(1 - \frac{a}{A}\right)\right] \quad \text{(J)}, \qquad 14.$$

where a is the initial area of the mixed region and A is its area after spreading. Because $a/A = 1$ before spreading, for complete homogenization, $\Delta GPE_{\text{r}} = (1/12)\rho_0 h^3 a N_0^2$. As spreading proceeds, $a/A \to 0$ and $\Delta GPE_{\text{r}} \to (1/24)\rho_0 h^3 a N_0^2$, half the initial value. If R_{f}^0 is the average during mixing, spreading reduces the ratio to

$$\lim_{a/A \to 0} R_{\text{f}} = \frac{R_{\text{f}}^0}{2 - R_{\text{f}}^0} \qquad 15.$$

(Arneborg 2002). Thus, if $R_{\text{f}}^0 = 0.2$, the net flux Ri_{g} will be 0.11, which Arneborg recommended for future use, noting that the reduced value should be consistent with tracer releases but not with microstructure measurements.

Simulating collapse of a mixed region with a half radius L, Lelong & Sundermeyer (2005) found that, after initial radial spreading, further expansion and circulation are strongest when $R_{\text{def}}/L \approx 1$, where R_{def} is the deformation radius. During the first half-inertial period, more than 70% of the initial potential energy was converted to kinetic energy before damped oscillations began generating internal waves. As the oscillations died, the energy partition was

$$PE_0 = \underbrace{PE_{\text{vortex}}}_{0.45} + \underbrace{KE_{\text{vortex}}}_{0.20} + \underbrace{PE_{\text{iw}}}_{0.10} + \underbrace{KE_{\text{iw}}}_{0.25}, \qquad 16.$$

with the ratio PE_{vortex}/PE_0 very close to the limit in Equation 14. This, however, does not include mixing from the shear of the vortex and radiating internal waves.

SUMMARY POINTS

1. It has long been understood that mixing efficiency is unlikely to be constant, but K_ρ from tracers and microstructure evaluated with $\gamma_{R_{\text{f}}} = \gamma_{\chi\epsilon} = 0.2$ agree better than do coefficients and efficiencies from simulations and experiment. The reasons for this agreement are not understood, particularly in view of the loss of potential energy from differential diffusion and mixed-region collapse being part of the diffusivity estimated with tracers but not of diffusivities derived from microstructure. Nonetheless, observations should continue to be scaled with 0.2 until observations, laboratory experiments, and numerical simulations converge on a more accurate formulation. In the meantime, published results should include as many parameters as possible to aid in understanding efficiency and allow subsequent recalculation of K_ρ.

2. Although much has been learned, substantial disagreements remain about mixing efficiency and coefficients, with estimates varying up to fivefold. Comparisons are complicated by too many definitions.
3. Observational estimates of $\gamma_{\chi\epsilon}$ sometimes have tight error bars for one ensemble, but no useful patterns emerge from the collection of reported estimates. This likely results from measurement errors and biases as well as dependencies on unreported parameters.
4. Functional dependencies of mixing efficiency and mixing coefficients should not be parameterized solely in terms of Re_b. Dimensional analysis and basic physics suggest the importance of other parameters, such as the gradient Richardson number, Ri_g, and the Reynolds number, Re. As a minimum, ϵ and N^2 distributions should be examined to ensure that large Re_b are not biased toward weak stratification.
5. Observations have not determined whether Kelvin-Helmholtz instabilities on sheared interfaces are the primary mechanism producing mixing in the ocean or just one of several instabilities by which internal waves break. Contrary to the implied sheet-and-layer structure of fine-scale stratification assumed for many simulations, most of the stratification is irregular and transient; high-gradient regions are usually bounded by less stratified layers, allowing overturns to generate internal wave energy that can propagate away from the breaking region.
6. Most turbulence produced by background internal waves is characterized by $Re_b \lesssim 200$, a range where significant departures from isotropy are expected.
7. The issues involved with mixing efficiency are nearly all based on assumptions of a linear Boussinesq fluid and appear to be of minor importance relative to the consequences of the nonlinear, non-Boussinesq nature of seawater.
8. The loss of potential energy by collapse and spreading of mixed regions is largely absent from applications of mixing efficiency to the pycnocline. Estimates of 50% loss indicate that mixing efficiency cannot be estimated solely from microstructure observations or mixing simulations that do not account for collapse.
9. Continuing the present approach relying on stand-alone observations, laboratory experiments, and models is unlikely to lead to a common understanding of mixing efficiency.

FUTURE ISSUES

1. A community effort is needed to focus observational, laboratory, and numerical approaches to mixing efficiency and mixing coefficients. To focus laboratory and numerical studies on relevant mechanisms and intensities, endeavors should begin with determining the mechanisms producing mixing in the ocean.
2. A few standard definitions should be adopted for mixing efficiency and mixing coefficients. We recommend focusing on instantaneous efficiency, $\mathcal{E}_i$; cumulative efficiency, $\mathcal{E}_c$; the flux Richardson number, R_f; and the mixing coefficient for K_ρ, $\gamma_{\chi\epsilon}$.

3. Accurate estimation of $\gamma_{\chi\epsilon}$ requires sensors with improved spatial responses that are the same from probe to probe as well as development of common calibration and analysis procedures and algorithms. A parallel development is needed for χ_S; owing to the strong likelihood that salt fingering and differential diffusion are significant in many locations, diapycnal diffusivity and mixing efficiency will remain ambiguous until mixing measurements incorporate salt diffusion.
4. In addition to continuing to explore mixing at large Reynolds numbers, simulations are needed to address mixing events occurring in much of pycnocline, where internal waves are close to the canonical Garrett and Munk background level, $Pr = 7$–10 and $Sc = 90$–230. Driven by random internal wave fields, profiles are irregularly stratified, and Re_b is usually less than several hundred.
5. As supplements to the usual two-dimensional contours, numerical and laboratory studies should help identify mixing mechanisms in the ocean with displays mimicking parameters that can be observed at sea, e.g., profiles of shear, stratification, ϵ, and χ_T.
6. Owing to their potential importance, focused studies are needed on nonlinear and non-Boussinesq effects on mixing efficiency. Preliminary estimates suggest that these effects can be much larger than other uncertainties. In general, efficiencies can have values anywhere between zero (for a homogeneous fluid, i.e., infinite Fr) and $\approx$0.2 for high Re. The question is which of these values applies to the ocean and under what conditions; mixing efficiency may have a functional dependence. Existing in situ data say that 0.2 is closer to the right answer, but we do not know why. Until we understand the actual mixing processes, from energy input to dissipation, we cannot claim to understand how mixing occurs and its efficiency. A major gap is understanding 1–10-m-scale instabilities that set the turbulence parameters determining efficiency. The processes are undoubtedly not as simple as Kelvin-Helmholtz or Holmboe instabilities or the idealized problems addressed by laboratory or numerical studies. We thus do not know how relevant these studies are to ocean mixing. Focused efforts combining in situ measurements and numerical modeling of those observations are needed.
7. A full understanding of mixing efficiency must be integrated with global energy balances seeking to understand how winds and tides drive water mass transformation (Wunsch & Ferrari 2004). For instance, energy inputs to an ocean mixed by high dissipation rates and low efficiency will differ markedly from those required by moderate dissipation rates and efficiency.

DISCLOSURE STATEMENT

The authors are not aware of any affiliations, memberships, funding, or financial holdings that might be perceived as affecting the objectivity of this review.

ACKNOWLEDGMENTS

Sutanu Sarkar, Ali Mashayek, Jim Moum, and Matthew Alford made useful suggestions, and Bill Smyth and Ren-Chieh Lien provided detailed, insightful comments. Rocky Geyer improved the result considerably with a thoughtful review.

LITERATURE CITED

Alford MH, Gregg MC, D'Asaro EA. 2005. Mixing, 3-D mapping and Lagrangian evolution of a thermohaline intrusion. *J. Phys. Oceanogr.* 35:1689–711

Alford MH, Pinkel R. 2000. Observations of overturning in the thermocline: the context of ocean mixing. *J. Phys. Oceanogr.* 30:805–32

Arneborg L. 2002. Mixing efficiencies in patchy turbulence. *J. Phys. Oceanogr.* 31:1496–506

Barry M, Ivey G, Winters K, Imberger J. 2001. Measurements of diapycnal diffusivities in stratified fluids. *J. Fluid Mech.* 442:267–91

Batchelor GK. 1959. Small-scale variation of convected quantities like temperature in turbulent fluid. Part 1. General discussion and the case of small conductivity. *J. Fluid Mech.* 5:113–39

Billant P, Chomaz J-M. 2001. Self-similarity of strongly stratified inviscid flows. *Phys. Fluids* 13:1645

Bouruet-Aubertot P, Koudella C, Staquet C, Winters K. (2001). Particle dispersion and mixing by breaking internal gravity waves. *Dyn. Atmos. Ocean* 33:95–134

Brucker K, Sarkar S. 2007. Evolution of an initially turbulent stratified shear layer. *Phys. Fluids* 10:105105

Carpenter J, Lawrence G, Smyth W. 2007. Evolution and mixing of asymmetric Holmboe instabilities. *J. Fluid Mech.* 582:103–32

Caulfield C, Peltier W. 2000. The anatomy of the mixing transition in homogenous and stratified free shear layers. *J. Fluid Mech.* 413:1–47

de Bruyn Kops S. 2015. Classical scaling and intermittency in strongly stratified Boussinesq turbulence. *J. Fluid Mech.* 775:436–63

Desaubies Y, Gregg MC. 1981. Reversible and irreversible finestructure. *J. Phys. Oceanogr.* 11:541–56

Desaubies Y, Smith W. 1982. Statistics of Richardson number and instability in oceanic internal waves. *J. Phys. Oceanogr.* 12:1245–59

Dillon TM. 1982. Vertical overturns: a comparison of Thorpe and Ozmidov length scales. *J. Geophys. Res.* 87:9601–13

Drazin P. 1977. On the instability of an internal gravity wave. *Proc. R. Soc. Lond. A* 356:411–32

Dunkerton T. 1997. Shear instability of internal inertial-gravity waves. *J. Atmos. Sci.* 54:1628–41

Ellison T. 1957. Turbulent transport of heat and momentum from an infinite rough plane. *J. Fluid Mech.* 2:456–66

Ferrari R, Polzin K. 2005. Finescale structure of the T-S relation in the eastern North Atlantic. *J. Phys. Oceanogr.* 35:1437–54

Fleury M, Lueck R. 1994. Direct heat flux estimates using a towed vehicle. *J. Phys. Oceanogr.* 24:801–18

Fringer O, Street R. 2003. The dynamics of breaking progressive interfacial waves. *J. Fluid Mech.* 494:319–53

Gargett A. 2003. Differential diffusion: an oceanographic primer. *Prog. Oceanogr.* 56:559–70

Gargett A, Moum J. 1995. Mixing efficiencies in turbulent tidal fronts: results from direct and indirect measurements of density flux. *J. Phys. Oceanogr.* 25:2583–608

Gargett A, Merryfield W, Holloway G. 2003. Direct numerical simulation of differential scalar diffusion in three-dimensional stratified turbulence. *J. Phys. Oceanogr.* 33:1758–82

Gargett AE, Osborn TR, Nasmyth PW. 1984. Local isotropy and the decay of turbulence in a stratified fluid. *J. Fluid Mech.* 144:231–80

Garrett CJR. 1984. Turning points in universal speculation on internal waves. In *A Celebration in Geophysics and Oceanography – 1982*, ed. CJR Garrett, C Wunsch, pp. 38–46. La Jolla, CA: Scripps Inst. Oceanogr.

Garrett CJR, Munk WH. 1975. Space-time scales of internal waves: a progress report. *J. Geophys. Res.* 80:291–97

Gregg MC. 1975. Microstructure and intrusions in the California Current. *J. Phys. Oceanogr.* 5:253–78

Gregg MC. 1989. Small-scale mixing: a first-order process? In *Parameterization of Small-Scale Processes: Proceedings, 'Aha Huliko'a Hawaiian Winter Workshop, University of Hawaii at Manoa, January 17–20, 1989*, ed. P Müller, D Henderson, pp. 117–26. Honolulu: Hawaii Inst. Geophys.

Gregg MC, D'Asaro EA, Shay T, Larson N. 1986. Observations of persistent mixing and near-inertial internal waves. *J. Phys. Oceanogr.* 16:856–85

Gregg MC, Horne J. 2009. Turbulence, acoustic backscatter and pelagic nekton in Monterey Bay. *J. Phys. Oceanogr.* 39:1097–114

Gregg MC, Sanford TB. 1988. The dependence of turbulent dissipation on stratification in a diffusively stable thermocline. *J. Geophys. Res.* 93:12381–92

Hamilton J, Lewis M, Ruddick B. 1989. Vertical fluxes of nitrate associated with salt fingers in the world's ocean. *J. Geophys. Res.* 94:2137–45

Hebert D. 1988. Estimates of salt-finger fluxes. *Deep-Sea Res. A* 35:1887–901

Henyey FS, Wright J, Flatté SM. 1986. Energy and action flow through the internal wave field: an eikonal approach. *J. Geophys. Res.* 91:8487–95

Holleman R, Geyer W, Ralston D. 2016. Stratified turbulence and mixing efficiency in a salt wedge estuary. *J. Phys. Oceanogr.* 46:1769–83

Inoue R, Smyth W. 2009. Efficiency of mixing forced by unsteady shear flow. *J. Phys. Oceanogr.* 39:1150–66

Ivey G, Imberger J. 1991. On the nature of turbulence in a stratified fluid. Part I: the energetics of mixing. *J. Phys. Oceanogr.* 21:650–58

Jackson PR, Rehmann CR. 2003. Laboratory measurements of differential diffusion in a diffusively stable, turbulent flow. *J. Phys. Oceanogr.* 33:1592–603

Jacobitz F, Sarkar S, Van Atta CW. 1997. Direct numerical simulations of the turbulence evolution in a uniformly sheared and stably stratified flow. *J. Fluid Mech.* 342:231–61

Jayne S. 2009. The impact of abyssal mixing parameterizations in an ocean general circulation model. *J. Phys. Oceanogr.* 39:1756–75

Kraichnan R. 1968. Small-scale structure of a scalar field convected by turbulence. *Phys. Fluids* 11:945–53

Kunze E. 2011. Fluid mixing by swimming organisms in the low-Reynolds-number limit. *J. Mar. Res.* 69:591–601

Kunze E. 2017. Internal-wave-driven mixing: global geography and budgets. *J. Phys. Oceanogr.* 47:1325–45

Kunze E, MacKay C, McPhee-Shaw E, Morrice K, Girton J, Terker S. 2012. Turbulent mixing and exchange with interior waters on sloping boundaries. *J. Phys. Oceanogr.* 42:910–27

Lazier J. 1973. Temporal changes in some fresh water temperature structures. *J. Phys. Oceanogr.* 3:226–29

Ledwell J, Duda T, Sundermeyer M, Seim H. 2004. Mixing in a coastal environment: 1. A view from dye dispersion. *J. Geophys. Res.* 109:C10013

Ledwell J, Laurent LS, Girton J, Toole J. 2011. Diapycnal mixing in the Antarctic Circumpolar Current. *J. Phys. Oceanogr.* 41:241–46

Ledwell J, Montgomery E, Polzin K, Laurent LCS, Schmitt R, Toole J. 2000. Evidence for enhanced mixing over rough topography in the abyssal ocean. *Nature* 403:179–82

Ledwell J, Watson A, Law C. 1998. Mixing of a tracer in the pycnocline. *J. Geophys. Res.* 103:21499–529

Lelong M-P, Dunkerton T. 1998a. Inertia–gravity wave breaking in three dimensions. I. Convectively unstable waves. *J. Atmos. Sci.* 55:2489–501

Lelong M-P, Dunkerton T. 1998b. Inertia–gravity wave breaking in three dimensions. II. Convectively stable waves. *J. Atmos. Sci.* 55(15):2473–88

Lelong M-P, Sundermeyer M. 2005. Geostrophic adjustment of an isolated diapycnal mixing event and its implications for small scale lateral dispersion. *J. Phys. Oceanogr.* 35:2352–67

Lilly D. 1983. Stratified turbulence and the mesoscale variability of the atmosphere. *J. Atmos. Sci.* 40:749–61

Lombard P, Riley JJ. 1996a. Instability and breakdown of internal gravity waves. I. Linear stability analysis. *Phys. Fluids* 8:3271

Lombard P, Riley JJ. 1996b. On the breakdown into turbulence of propagating internal waves. *Dyn. Atmos. Ocean* 23:345–55

Maffioli A, Brethouwer G, Lindborg E. 2016. Mixing efficiency in stratified turbulence. *J. Fluid Mech.* 794:R3

Mashayek A, Caulifield C, Peltier W. 2013. Time-dependent, non-monotonic mixing in stratified turbulent shear flows: implications for oceanographic estimates of buoyancy flux. *J. Fluid Mech.* 736:570–93

Mashayek A, Peltier W. 2011. Three-dimensionalization of the stratified mixing layer at high Reynolds number. *Phys. Fluids* 23:111701

Mashayek A, Peltier W. 2013. Shear-induced mixing in geophysical flows: Does the route to turbulence matter to its efficiency? *J. Fluid Mech.* 725:216–17

Mater B, Venayagamoorthy S. 2014. A unifying framework for parameterizing stably stratified shear-flow turbulence. *Phys. Fluids* 26:036601

McComas C, Müller P. 1981. The dynamic balance of internal waves. *J. Phys. Oceanogr.* 11:970–86
McEwan A. 1983a. Internal mixing in stratified fluids. *J. Fluid Mech.* 128:59–80
McEwan A. 1983b. The kinematics of stratified mixing through internal wavebreaking. *J. Fluid Mech.* 128:47–57
McPhee MG. 1992. Turbulent heat flux in the upper ocean under sea ice. *J. Geophys. Res.* 97:5365–79
Merryfield W. 2005. Dependence of differential mixing on n and R_p. *J. Phys. Oceanogr.* 35:991–1003
Mied R. 1976. The occurrence of parametric instabilities in finite-amplitude internal gravity waves. *J. Fluid Mech.* 78:763–84
Moum J. 1996. Efficiency of mixing in the main thermocline. *J. Geophys. Res.* 101:12057–69
Moum JN, Caldwell DR, Paulson CA. 1989. Mixing in the equatorial surface layer and thermocline. *J. Geophys. Res.* 94:2005–21
Nash J, Moum J. 2002. Microstructure estimates of turbulent salinity flux and the dissipation spectrum of salinity. *J. Phys. Oceanogr.* 32:2312–34
Oakey N. 1982. Determination of the rate of dissipation of turbulent energy from simultaneous temperature and velocity shear microstructure measurements. *J. Phys. Oceanogr.* 12:256–71
Oakey N. 1985. Statistics of mixing parameters in the upper ocean during JASIN Phase 2. *J. Phys. Oceanogr.* 15:1662–75
Oakey N, Greenan B. 2004. Mixing in a coastal environment: 1. A view from microstructure measurements. *J. Geophys. Res.* 109:C10014
Osborn TR. 1974. Vertical profiling of velocity microstructure. *J. Phys. Oceanogr.* 4:109–15
Osborn TR. 1980. Estimates of the local rate of vertical diffusion from dissipation measurements. *J. Phys. Oceanogr.* 10:83–89
Osborn TR, Cox C. 1972. Oceanic fine structure. *Geophys. Fluid Dyn.* 3:321–45
Peltier W, Caulfield C. 2003. Mixing efficiency in stratified shear flows. *Annu. Rev. Fluid Mech.* 35:135–67
Peters H, Gregg MC. 1988. Some dynamical and statistical properties of equatorial turbulence. In *Small-Scale Turbulence and Mixing in the Ocean: Proceedings of the 19th International Liège Colloquium on Ocean Hydrodynamics*, ed. J Nihoul, B Jamart, pp. 185–200. Amsterdam: Elsevier
Peters H, Gregg MC, Sanford TB. 1995. Detail and scaling of turbulent overturns in the Pacific Equatorial Undercurrent. *J. Geophys. Res.* 100:18349–68
Pham H, Sarkar S. 2010. Transport and mixing of density in a continuously stratified shear layer. *J. Turbul.* 11:N24
Pham H, Sarkar S, Brucker K. 2009. Dynamics of a stratified shear layer above a region of uniform stratification. *J. Fluid Mech.* 630:191–223
Pinkel R, Anderson S. 1992. Toward a statistical description of finescale strain in the thermocline. *J. Phys. Oceanogr.* 22:773–95
Polzin K, Toole J, Schmidt R. 1995. Finescale parameterization of turbulent dissipation. *J. Phys. Oceanogr.* 25:306–28
Pope S. 2000. *Turbulent Flows*. Cambridge, UK: Cambridge Univ. Press
Pujiana K, Moum J, Smyth W, Warner S. 2015. Distinguishing ichthyogenic turbulence from geophysical turbulence. *J. Geophys. Res.* 120:3792–804
Riley JJ, de Bruyn Kops SM. 2003. Dynamics of turbulence strongly influenced by buoyancy. *Phys. Fluids* 15:2047–59
Riley JJ, Lelong M-P. 2000. Fluid motions in the presence of strong stable stratification. *Annu. Rev. Fluid Mech.* 32:613–57
Rohr JJ, Itsweire EC, Van Atta CW. 1984. Mixing efficiency in stably stratified decaying turbulence. *J. Fluid Mech.* 29:221–336
Ruddick B, Walsh D, Oakey N. 1997. Variations in apparent mixing efficiency in the North Atlantic central water. *J. Phys. Oceanogr.* 27:2589–605
Salehipour H, Caulfield C, Peltier W. 2016. Turbulent mixing due to the Holmboe wave instability at high Reynolds number. *J. Fluid Mech.* 803:591–621
Salehipour H, Peltier W. 2015. Diapycnal diffusivity, turbulent Prandtl number and mixing efficiency in Boussinesq stratified turbulence. *J. Fluid Mech.* 775:464–500

Salehipour H, Peltier W, Mashayek A. 2015. Turbulent diapycnal mixing in stratified shear flows: the influence of Prandtl number on mixing efficiency and transition at high Reynolds number. *J. Fluid Mech.* 773:178–223

Schmitt R. 1981. Form of the temperature-salinity relationship in the central water: evidence for double-diffusive mixing. *J. Phys. Oceanogr.* 11:1015–26

Scotti A, White B. 2016. The mixing efficiency of stratified turbulent boundary layers. *J. Phys. Oceanogr.* 46:3181–91

Seim HE, Gregg MC. 1994. Detailed observations of a naturally occurring shear instability. *J. Geophys. Res.* 99:10049–73

Sherman J, Davis R. 1995. Observations of temperature microstructure in NATRE. *J. Phys. Oceanogr.* 25:1913–29

Shih L, Koseff J, Ivey G, Ferziger J. 2005. Parameterization of turbulent fluxes and scales using homogenous sheared stably stratified turbulence simulations. *J. Fluid Mech.* 525:193–214

Smith J. 1974. Turbulent structure of the surface boundary layer in an ice-covered ocean. *Rapp. P.-V. Réun. Cons. Int. Explor. Mer* 167:53–65

Smyth W, Carpenter J, Lawrence G. 2007. Mixing in symmetric Holmboe waves. *J. Phys. Oceanogr.* 37:1566–83

Smyth W, Moum J. 2000. Anisotropy of turbulence in stably stratified mixing layers. *Phys. Fluids* 12:1343–62

Smyth W, Moum J. 2012. Ocean mixing by Kelvin-Helmholtz instability. *Oceanography* 25(2):140–49

Smyth W, Moum J, Caldwell D. 2001. The efficiency of mixing in turbulent patches: inferences from direct simulations and microstructure observations. *J. Phys. Oceanogr.* 31:1969–92

Smyth W, Nash J, Moum J. 2005. Differential diffusion in breaking Kelvin-Helmholtz billows. *J. Phys. Oceanogr.* 35:1004–1002

Smyth W, Winters K. 2003. Turbulence and mixing in Holmboe waves. *J. Phys. Oceanogr.* 33:694–711

St. Laurent L, Schmitt R. 1999. The contribution of salt fingers to vertical mixing in the North Atlantic Tracer Release Experiment. *J. Phys. Oceanogr.* 29:1404–24

Staquet C. 2000. Mixing in a stably stratified shear layer: two- and three-dimensional numerical experiments. *Fluid Dyn. Res.* 27:367–404

Strang E, Fernando H. 2001. Entrainment and mixing in stratified shear flows. *J. Fluid Mech.* 428:349–86

Tailleux R. 2009a. On the energetics of stratified turbulent mixing, irreversible thermodynamics, Boussinesq models and the ocean heat engine controversy. *J. Fluid Mech.* 638:339–82

Tailleux R. 2009b. Understanding mixing efficiency in the ocean: Do the nonlinearities of the equation of state for seawater matter? *Ocean Sci.* 5:271–83

Thorpe S. 1973. Experiments on instability and turbulence in a stratified shear flow. *J. Fluid Mech.* 61:731–51

Toole J, Polzin K, Schmitt R. 1994. Estimates of diapycnal mixing in the abyssal ocean. *Science* 264:1120–23

Turner J. 1968. The influence of molecular diffusivity on turbulent entrainment across a density interface. *J. Fluid Mech.* 33:639–56

Whalen C, MacKinnon J, Talley L, Waterhouse A. 2015. Estimating the mean diapycnal mixing using a finescale strain parameterization. *J. Phys. Oceanogr.* 45:1174–88

Wijesekera H, Dillon T. 1997. Shannon entropy as an indicator of age for turbulent overturns in the oceanic thermocline. *J. Geophys. Res.* 102:3279–91

Winters K, D'Asaro EA. 1996. Diascalar flux and the rate of fluid mixing. *J. Fluid Mech.* 317:179–93

Winters K, Lombard P, Riley JJ, D'Asaro EA. 1995. Available potential energy and mixing in density-stratified fluids. *J. Fluid Mech.* 289:115–28

Woods J. 1968. Wave-induced shear instability in the summer thermocline. *J. Fluid Mech.* 32:791–800

Woods J, Wiley R. 1972. Billow turbulence and ocean microstructure. *Deep-Sea Res. Oceanogr. Abstr.* 19:87–121

Wunsch C, Ferrari R. 2004. Vertical mixing, energy, and the general circulation of the oceans. *Annu. Rev. Fluid Mech.* 36:281–314

Yamazaki H, Osborn TR. 1990. Dissipation estimates for stratified turbulence. *J. Geophys. Res.* 95:9739–44

Yamazaki H, Osborn TR. 1993. Direct estimation of heat flux in a seasonal thermocline. *J. Phys. Oceanogr.* 23:503–16